Anhedonic behaviour in a TLR7-driven neuroinflammation mouse model is associated with impaired thalamostriatal signalling and immune cell ingress into the brain

Deepika Sharma[1,+], Lilya Andrianova[1,2,+], Rhona McGonigal[1,+], Kirstyn Gardner-Stephen[1], Hassan al Fadhel[1], Jennifer A Barrie[1], Richard Hohne[1], Megan Saathoff[1,3], Yaprak Karabalci[2], Julie-Myrtille Bourgognon[1,2], John J Cole[3], Michael T Craig[2,*], Jonathan T Cavanagh[1,*]

[+]contributed equally

*corresponding author

[1] School of Infection & Immunity, College of Medical, Veterinary & Life Sciences, Sir Graham Davies Building, University of Glasgow, Glasgow G12 8QQ. UK

[2] School of Psychology & Neuroscience, College of Medical, Veterinary & Life Sciences, Sir James Black Building, University of Glasgow, Glasgow G12 8QQ. UK

[3] Molecular Analysis, MVLS Shared Research Facilities, College of Medical, Veterinary & Life Sciences, Joseph Black Building, University of Glasgow, Glasgow G12 8QQ. UK.

Correspondence to Jonathan.cavanagh@glasgow.ac.uk or mick.craig@glasgow.ac.uk

Keywords: Synaptic transmission, Anhedonia, Depression, Neuroinflammation, T cell biology, Glia, Thalamus, Striatum, Neurobiology, Immunology

Abstract

Depression is a heterogenous condition driven by multiple aetiologies, which make its pathophysiology challenging to map. Stratifying depression by underlying biological causes may allow for more effective, targeted treatments. Immune-mediated inflammation is present in around 20% of individuals with depression and provides a potential mechanistic pathway for some key symptoms such as reward / hedonic impairment. Here we used a non-invasive model of neuroinflammation, topical application of Aldara (a TLR7/8 agonist) for 3 days in mice, to explore relationships between the intracerebral immune response, neural circuitry and behaviours closely linked to depression: motivation, reward and anxiety.

Mice that were treated with Aldara exhibited anhedonia-like behaviour and impairments in intrinsic motivational behaviours (measured through assays such as sucrose preference and nest-building tests) relative to untreated controls, but displayed little anxiety-like behaviour. Aldara-driven neuroinflammation was associated with evidence of immune cell (including lymphoid and myeloid cells) ingression into the brain, and both microglia and astrocytes showed evidence of activation. Within 4 to 6 hours of Aldara treatment, neurons in midline thalamus showed strongly increased Fos immunoreactivity relative to controls. Optogenetic activation of midline thalamic projections onto ventral striatum medium spiny neurons (MSNs) revealed that Aldara treatment substantially reduced the magnitude of the evoked thalamic AMPA receptor-mediated EPSC, but with no change to the AMPA/NMDA ratio nor change in the frequency of amplitude of spontaneous EPSP. Finally, whole brain transcriptome overrepresentation analysis revealed that Aldara treatment led to significant upregulation of genes associated with immune response and downregulation of genes associated with glutamate metabolism and synaptic transmission.

Altogether, our data suggest potential, testable mechanisms through which neuroinflammation can drive anhedonic-like behaviour through activation of resident neural cells, infiltrating activated immune cells and functional changes in thalamostriatal circuitry consistent with increased extrasynaptic glutamate.

Introduction

Among the most important recent developments in neuroscience has been the discovery of the role played by brain-immune interactions in the aetiology of conditions including dementia (*1*) and schizophrenia (*2*), as well the progression of acute neurological insults such as stroke and traumatic brain injury (*3*). Chronic inflammation also appears to contribute to the pathophysiology of depression, with up to almost 50% of patients with immune-mediated inflammatory disease (IMIDs) such as rheumatoid arthritis, experiencing comorbid depression (reviewed by *4*). Treatment with immune therapies that target key inflammatory molecules such as TNFα, or IL-17 also alleviate the comorbid depression in IMIDs for some, but not all, patients (see *5* for our recent review). The behavioural consequences of neuroinflammation in humans include a negative impact on mood/reward responses, anxiety, energy levels and cognition. While well-recognized, these phenotypes are ubiquitous and have almost no targeted therapies. As such they represent a major unmet clinical need, the mechanisms for which remain opaque; discovering the neurobiological basis of immune-mediated behaviour is a necessary pre-requisite to developing novel therapeutics.

Neuroinflammation results in upregulation of proinflammatory cytokines and chemokines within the brain, which can then perturb neural function through numerous mechanisms. For example, chronic mild stress in rats drives anhedonic behaviour and is associated with increased TNFα and IL-1β in hypothalamus (*6*), and lipopolysaccharide (LPS) administration is widely used to model inflammation-mediated depression in mice (*7*). TNFα can inhibit the uptake of glutamate in primary astrocytes (*8*) as well as driving its release from microglia (*9*). TNFα can also act directly on TNFR1 receptors on neurons to alter AMPA and GABA receptor trafficking within minutes of TNFα application in culture (*10*). The precise neurobiological mechanisms, through which neuroinflammation can drive depression and anhedonia in humans are, however, still unclear. Analogous behaviours can also be observed in well-validated rodent models, affording an opportunity to explore these mechanisms.

In the present study, we aimed to address the research question: what molecular and cellular changes occur in the brain due to neuroinflammation, and how does this immune activity affect neural

circuitry of motivation? Many animal models of neuroinflammation involve acute peripheral stimuli, such as treatment with LPS or poly I:C, which tend to drive a very strong immune response mimicking bacterial or viral infection, respectively. It is not clear whether these strong, acute immune activations drive similar or distinct mechanisms from the low-level chronic immune activation seen in humans with IMID. We have therefore used a TLR7/8 agonist (Aldara™; active ingredient 5% Imiquimod [IMQ]) that directly accesses the brain and provides a non-invasive sub-chronic model of neuroinflammation. By deploying a broad array of immunology and neuroscience methods, here we describe the effects of neuroinflammation on gene expression, peripheral immune cell infiltration into the CNS, brain resident cells activation, and describe cellular and synaptic changes that occur in the brain alongside reduced motivational behaviour.

Material and Methods

Mice

Female C57BL/6J mice were obtained from Charles River Laboratories (UK) and housed in individual ventilated cages. Animals underwent acclimatisation for one week prior to experimental use at 8 to 10 weeks of age (group numbers are described per experiment below). Animals were maintained in a 12 h light/dark cycle in controlled temperature and humidity with *ad libitum* access to food and water. All experiments were carried out in accordance with the UK Animal (Scientific Procedures) Act 1986 and were subject to local ethical approval by the University of Glasgow Animal Welfare and Ethical Review Board.

Aldara model

C57BL/6 female mice (8 to 10 weeks old, starting weight range: 16.3 – 23.3g) were each treated with a ~62.5 mg dose of Aldara™ (Meda AB, UK) cream containing 5% IMQ or an equivalent volume of control cream (Boots Aqueous Cream B.P.; Boots Pharmacy, UK) by topical application to shaved dorsal skin near the base of the tail (~3mm^2 area). Treatment was applied for 3 consecutive days,

with tissue collected 24h after the final application. Soft diet was provided to both control and experimental groups and mice monitored daily for weight loss. Female mice only were used in this study due to male mice showing differences in inflammatory response to topical application of inflammatory agents, as we discuss in our previous work using this model (*11*).

Experimental design

Mice were randomly allocated to treatment groups. A power analysis was performed using G*Power (*12*) software (v3.0.10 G*Power, RRID:SCR_013726) to determine minimum group size; n = 4/5 (immunostaining), n = 4 (flow) and n = 8 (behaviour) were selected for each treatment group. The effect size for output was based on previous or pilot experiments, with calculations made on a basis of 80% power, and a significance criteria of 0.05. All tissue was coded prior to imaging and analysis to prevent researcher bias.

Statistical analysis

Unless otherwise stated, the numbers of independent animals are described per experiment above and indicated in the figure legends. Statistical differences were determined using GraphPad Prism software (GraphPad Prism, RRID:SCR_002798).

Flow cytometry

Mice were given a terminal overdose of the anaesthetic sodium pentobarbitone (Euthatal, 10 µl/g of 200 mg/ml solution) and, once deeply anaesthetised, were killed by transcardial perfusion with 20 ml of ice-cold PBS. Whole brains were dissociated using the Adult Brain Dissociation Kit for mouse (Miltenyi Biotech: Cat. No.:130-107-677, UK) in line with manufacturer's instructions. Briefly, whole brains were cut into 8-10 pieces and placed into a C-tube containing the enzyme mix. Samples were dissociated in the gentleMACSTM Octo Dissociator with heaters using program 37C_ABDK_01 (Miltenyi, UK). Subsequently, samples were filtered through a 70 µm strainer using 10 ml of D-PBS and the back of a 5 ml syringe plunger before being spun at 300 g for 1 0min, 4ºC. The supernatant was discarded, and cells were re-suspended in 3.1 ml D-PBS and 900 µL Debris Removal Solution.

Another 4 ml of D-PBS was overlain gently, and samples were spun at 3,000 g for 10 min, 4ºC, with half (5) acceleration and half (5) brake. The top two phases, containing debris and myelin, were removed and discarded. D-PBS was added, and cells were centrifuged at 1,000 g for 10 min, 4ºC, and supernatant discarded. Erythrocytes were removed by incubating with 1X Red Blood Cell Removal Solution (provided in the kit) diluted in water for 10min at 4ºC before adding cold PB Buffer. Samples were spun again at 300 g for 10 min, 4ºC and the pellet was dissolved in 1 ml of PBS. Trypan blue and hemacytometer were used for cell counting.

Brain cells were stained in 96-well plate, following protocol with FACS (2% FBS and 0.4% of 50 mM EDTA in 1X PBS) buffer wash and centrifuge spin (400g for 5min at 4ºC) in between each step (all incubations were performed at 4ºC unless stated otherwise). Live/dead staining (eBioscience™ eFluor™ 506 Catalog number: 65-0866-14, USA) was done in PBS for 20 mins. Fc block (Miltenyi, 130-059-901, UK) step was done for 20 mins and conjugated extracellular antibody (see supplementary table) staining was done in FACS buffer for 20 mins. For intracellular staining, single cells, post extracellular staining, were stimulated with cell stimulation cocktail with protein transport inhibitor (eBioscience™ Cell Stimulation Cocktail (plus protein transport inhibitors) (500X) cat. No. 00-4975-03, USA) for 4 hours at 37 C° in CO_2 incubator. Cells were fixed (Fix buffer, BD Biosciences, USA cat no. 554655) and permeabilized with Perm buffer (BD Biosciences, USA cat. No. 554723) and intracellular staining (see supplementary table) was done in perm buffer. All fluorescence minus one (FMO) staining controls received the full panel staining except for one antibody to determine true populations in the sample (see supplementary material). FMOs were generated using pooled sample cells. Compensation was performed with antibody stained UltraComp eBeads (Thermo Fischer Scientific, USA, cat No. 01-2222-41). Flow cytometry was performed at the Flow Core Facility (University of Glasgow) on the LSR Fortessa (BD Biosciences, USA). Data is acquired through BD FACSDiVaTM digital software. All analysis was performed using FlowJo software (v.10.10.0.) (BD Biosciences, USA). Graphs were generated using absolute cell number using the cell counts from hemocytometer and gating strategies percentages (see supplementary material).

RNA extraction & Bulk RNA Sequencing

Following PBS perfusion, as described above but under RNase-free conditions, brain hemispheres were moved to Qiazol Lysis Reagent (Qiagen) and homogenized using a TissueLyser LT (Qiagen) for 3 minutes with a 5 mm stainless steel ball (Qiagen, Cat. No. 69989). RNA was isolated using the Qiagen RNeasy Lipid Tissue Extraction Kit (Qiagen, Cat. No.: 74804) with RNeasy on-column treatment as per manufacturer's instructions. RNA quality was assessed using an Agilent 2100 Bioanalyzer (Agilent Technologies) at Glasgow Polyomics facility. Samples were stored at -80oC until Bulk RNAseq processing. Bulk RNA sequencing was completed by Novogene, with a read length of 2x150bp and an average of 53 million reads per sample. The data was aligned to the mouse genome (ensembl_mus_musculus_grcm38_p6_gca_000001635_8) using HiSat2 (*13*), with > 90% uniquely aligned concordant pairs per sample. Raw read counts were normalised and differential expression calculated using DESeq2 (*14*) using pairwise models with no additional covariates. The normalised data was explored using the Searchlight analysis platform, with the pipeline described in detail elsewhere (*15*). The significance threshold for differential genes was adjusted $p < 0.05$ and absolute log2fold > 0.5. All other parameters were left to default.

Overrepresentation analysis (ORA) and visualisation was carried out using G:Profiler (*16*) and the G:Profiler2 package (*17*) in R Statistical Software (v4.3.1; R Core Team 2023) in R Studio (Posit team (2023). RStudio: Integrated Development Environment for R. Posit Software, PBC, Boston, MA. URL http://www.posit.com/). For the ORA analysis in G:Profiler, we ordered the DE gene lists by most significant for upregulated and downregulated genes, and run ORA using the g:GOSt function with this ordered input against the *mus musculus* database. The significance threshold was set to adjusted $p < 0.05$ and only annotated genes were considered.

Immunohistochemistry

Mice were given a terminal overdose of the anaesthetic sodium pentobarbitone (Euthatal, 10 µl/g of 200 mg/ml solution) and, once deeply anaesthetised, were killed by transcardial perfusion with PBS followed by 4% paraformaldehyde (Sigma-Aldrich, UK). Following perfusion-fixation, whole brains

(n=4 / treatment) were dissected into 4% PFA overnight at 4°C, then cryoprotected in 30% sucrose at 4°C. Coronal sections were cut at 40µm on a SM2010R freezing microtome (Leica, UK) and collected into in-house solution of antifreeze (containing 30% ethylene glycol, 25% glycerol and 25% 0.2M PB in ddH_2O) and stored at -20°C until required. Free-floating sections were washed in PBS then treated with 100% EtOH at -20°C for 10 min, or an antigen retrieval method (overnight at 60°C in 10 mM sodium citrate buffer (pH 6.0)). Tissue was thoroughly washed in PBS, then blocked in PBS containing 10% normal goat serum (NGS) + 0.3% Triton X for 1h at 4°C. Primary antibodies were prepared in PBS containing 3% NGS and applied overnight (or 72 hours in the case of IBA-1 and GFAP) at 4°C. Primary antibodies included a combination of the following: rat anti-CD4 antibody (Biolegend, UK, cat# 100505, 1:500), guinea pig anti-IBA1 antibody (Synaptic Systems, Germany, Cat# 234 308, 1:500), rabbit anti-GFAP antibody (Novus Biologicals, UK, Cat# NB300-141, 1:500), rabbit anti-c-fos (Cell Signalling Technologies, UK, cat # 2250S, 1:500). Sections were washed 3x 10mins in PBS, before the appropriate combination of secondary antibodies were applied for 2h at RT. Secondary antibodies were as follows: isotype-specific Alexa Fluor 488- and Alexa Fluor 546-conjugated goat anti-rat IgG antibodies (Thermo Fisher Scientific Cat# A-21434, RRID:AB_2535855; 1/500), Alexa Fluor 488 goat anti-guinea pig (Abcam, UK, Cat# ab150185, 1:500), Alexa Fluor 594 goat anti-rabbit (Invitrogen, USA, Cat# A11012, 1:500). 3 x 10min PBS washes were followed by mounting in VECTASHIELD® HardSet™ mounting medium with DAPI (Vector Labs, UK, Cat# H-1500-10).

Anatomical tracing of the thalamostriatal projections

Mice that had undergone stereotaxic injections of viral vectors to transduce Chronos-GFP (details below) were killed by perfusion-fixation as described above. Coronal sections were sliced at 50 µm. The slices around the injection coordinates as well as positive control areas (such as prefrontal cortices) and experimental striatal slices were selected and underwent the immunofluorescent staining protocol described above. To enhance visualisation of thalamic axons, sections were incubated with primary antibody against GFP (chicken anti-GFP; Abcam, UK, cat # ab64905, 1:50000) followed by incubation with Alex488-conjugated goat anti-chicken secondary antibody

(Abcam, UK, cat # ab150173,1:250). Once stained, the slices were mounted using the HardSet mounting medium containing DAPI (VectorLabs, UK), and images were taken on SLM710 confocal microscope (Zeiss).

Image acquisition and analysis

For immune cell infiltration studies, tile scans of entire coronal brain sections were captured using a widefield inverted Leica DMi8 microscope with a 10x objective. FIJI (ImageJ) software (*18*) was used to analyse the images as follows: the DAPI channel was used to outline each selected brain region with reference to the Allen brain atlas. The number of CD4-positive cells within this measured area were counted per mouse, the mean plotted and compared per treatment for each region. Criteria for cell inclusion included CD4 positive signal, a DAPI nucleus and a diameter of 8-12 μm. Illustrative images were captures using a Zeiss LSM 880 Axio Imager 2 laser-scanning confocal microscope (Zeiss Microscopy, UK) processed using Zen Zeiss Microscopy Software.

For c-fos quantification in the thalamus, confocal z-stacks were captured using a Zeiss LSM 880 Axio Imager 2 laser-scanning confocal microscope equipped with an LD C-Apochromat 20x/1.1 W Korr M27 objective at 0.8 μm optical slice. The same exposure levels were used to capture images from all sections. Quantification of the number of Fos positive cells per ROI was performed in FIJI from maximum intensity z-projections.

For analysing the fluorescence signal intensities and coverage areas of IBA-1 and GFAP, confocal z-stack images of IBA-1 and GFAP immunofluorescence were acquired using a Zeiss LSM 880 Axio Imager 2 laser-scanning confocal microscope equipped with an LD C-Apochromat 40x/1.1 W Korr M27 objective (Zeiss, 421867-9970-000) and Immersol W 2010 immersion oil (Zeiss, 444969-0000-000). Each image stack consisted of 16 optical sections spaced 2 μm apart (total depth 30 μm) with a resolution of 2048 x 2048 pixels (354.25 μm x 354.25 μm).

To quantify IBA-1 and GFAP signal intensity and coverage area, the images were first processed the images to subtract the background signals using a 35-pixel rolling ball radius applied to each z-stack in fiji. Maximum intensity z-projections were then generated, and positive signals isolated using pre-trained pixel classifiers for IBA-1 and GFAP within the LabKit Fiji plugin (Arzt et al., 2022). The resulting binary masks were used to calculate the percentage area covered by positive signal and to redirect measurements to the original image to measure the mean grey value within the positive signal regions.

Stereotaxic surgeries

Several midline thalamic nuclei target ventral striatum including but not limited to paraventricular (PVT), centromedian (CM) and parataenial (PT) thalamic nuclei (*19*). To broadly target midline thalamus for optogenetic and electrophysiological experiments, we carried out stereotaxic injections to deliver 300 nl of AAV8-hSyn-Chronos-GFP (UNC Viral Vector Core, USA; contributed by Ed Boyden; titre 3.1×10^{13} viral particles / ml) to the border of CM and PVT. We used the following stereotaxic coordinates: R/C -0.5 mm and M/L 0 mm from Bregma, at a depth of 3.3 mm from the pial surface. Briefly, mice were anaesthetised with 5% Isoflurane, were placed on a heated pad for the duration of the surgery and maintained at 1.5–2.5% isoflurane (with a flow rate of ~2 l min^{-1} O_2). Mice were then subcutaneously dosed with 0.1 mg/kg of buprenorphine (buprenorphine hydrochloride, Henry Schein) and 5 mg/kg of carprofen (Rimadyl, Henry Schein) at the start of surgery, and additional doses of carprofen were provided subcutaneously subsequent days, as required. Anaesthetised mice were placed in a Kopf 940 Small Animal stereotaxic frame (David Kopf Instruments, CA, USA). An incision was made down the midline, and a craniotomy was performed to allow injection of virus (300 nl) using a Neuros Syringe (Hamilton Company, NV, USA) injected at a rate of 100 nl/min using a UMP3 UltraMicroPump (World Precision Instruments, UK). Mice were recovered for 3 weeks to allow sufficient time for opsin expression to occur before undergoing Aldara treatment as described above.

Electrophysiology experiments

Drugs and chemicals

CGP55845, DNQX, gabazine, DL-AP5 and picrotoxin were purchased from either Tocris Bioscience (UK) or HelloBio (UK), and all other chemicals were purchased from Sigma-Aldrich (UK) unless otherwise stated.

Brain slice preparation

Mice were deeply anesthetised with 5% isoflurane and the brain was rapidly dissected out in room temperature NMDG cutting solution, containing (in mM): 135 NMDG, 20 choline bicarbonate, 10 glucose, 1.5 $MgCl_2$, 1.2 KH_2PO_4, 1 KCl, 0.5 $CaCl_2$, saturated with 95% O_2 and 5% CO_2 (pH 7.3-7.4). Brains were hemisected and coronal slices (400 um) were cut using a VT-1200S vibratome (Leica Microsystems, Germany) and the slices were transferred into a chamber containing recording aCSF, composed of (in mM): 130 NaCl, 24 $NaHCO_3$, 3.5 KCl, 1.25 NaH_2PO_4, 2.5 $CaCl_2$, 1.5 $MgCl_2$, and 10 glucose, saturated with 95% O_2 and 5% CO_2 (pH 7.4. Slices were placed in a water bath at 37 °C for 30 minutes and slowly cooled to room temperature for further 30 minutes, at which they maintained until recording.

Patch-clamp recording

For *ex vivo* patch clamp recordings, slices were attached onto 0.1% poly-L-lysine (Sigma Aldrich, P8920) coated glass slides and placed into the upright microscope and visualized using infrared oblique contrast microscopy (Scientifica SliceScope, Scientifica, UK). A CoolLED pE-4000 system (CoolLED, UK) was used to confirm presence of thalamic axons in slices, and to provide optogenetic stimulation. The slices were submerged in recording aCSF, warmed to 32-34 °C, and the rate of perfusion was kept at 5 ml/min. The recording electrodes resistance was typically 4 – 6 MΩ and were pulled from borosilicate glass (World Precision Instruments, UK) using a Sutter P-1000 horizontal puller (Sutter Instruments, CA, USA). The intracellular solution used had the following composition (in mM): 135 Cs-methanesulphonate, 8 NaCl, 10 HEPES, 0.5 EGTA, 4 MgATP, 0.3 Na-GTP, 5 QX314, plus 2 mg/ml biocytin (VWR International, UK), at pH 7.25 adjusted with CsOH to 285 mOsm.

Whole-cell recordings in voltage clamp mode were made from ventral striatum targeting medium spiny neurons (MSNs) based on morphology. Gabazine (10 μM) and CGP55845 (1 μM) were present in the bath throughout recordings to block $GABA_A$ and $GABA_B$- receptor-mediated currents, respectively.

Upon formation of a whole-cell patch, spontaneous activity was recorded for 1 to 2 minutes to sample spontaneous EPSC activity, at a holding potential of -70 mV. A single light pulse was of 470 nm was then applied once every 10 seconds to optogenetically-excite midline thalamic inputs onto ventral MSNs. After a suitable baseline had been established (typically >20 sweeps), 10 μM of AMPA receptor antagonist DNQX was added to the bath to inhibit AMPA-mediated synaptic currents. The holding potential was then switched to +50 mV to allow recording of NMDA receptor-mediated synaptic currents. To confirm the presence of the NMDA current, D-AP5 (100 μM) was added at the end of the recording in a subset of recordings. Whole-cell patch-clamp recordings were made using a Multiclamp 700B amplifier (Molecular Devices, CA, USA). Signals were low-pass filtered at 8 kHz and digitized at 20 kHz using a Digidata 1440A and pClamp 10.2 (Molecular Devices, CA, USA). Recordings were not corrected for a liquid junction potential.

Data Analysis

Electrophysiology data were analysed in ClampFit 11 (Molecular Devices, CA, USA). To measure spontaneous EPSCs, traces were first band-pass filtered in using a high-pass 8 pole Bessel band pass filter 2Hz and a low-pass Gaussian filter at 1000Hz, and sEPSCs were detected using template matching. For evoked EPSC analysis, data were first baselined to zero and an average was taken of at least 20 traces for both AMPA- and NMDA- receptor-mediated components. The AMPA receptor-mediated EPSC was determined as the maximal EPSC peak at -70mV and NMDA receptor-mediated EPSC as the highest peak at +50 mV. For example trace figure preparation, recordings were imported into Igor Pro (Wavemetrics, OR) using Neuromatic (Thinkrandom, UK). Raw sEPSC traces were band-pass filtered in Igor Pro between 0.1 and 1000 Hz to improve clarity. GraphPad Prism (Graphpad, CA) was used for statistical analysis. Data were tested for normality using the

D'Agostino and Pearson test and subsequently analysed by parametric or nonparametric tests as appropriate. Unless otherwise stated, all values are presented as mean ± SEM.

Post hoc morphological recoveries

The tissue slices were post-fixed in 4% PFA solution for an hour after recordings and then transferred to PBS (Melford, UK). Slices were washed thrice in 0.1 M PBS solution, followed by three further washes in PBS with 0.5% Triton X (Sigma, UK). Two blocking steps were used: 100mM of Glycine (Sigma, UK) incubation for 20 mins and then 1-hour long incubation with blocking buffer with 10% goat serum (VectorLabs, UK) at room temperature. Primary antibody against GFP (Abcam, UK) at 1:5000 dilution was used overnight at 4°C; then secondary conjugated anti-chicken antibody (ab150173, Abcam UK) and streptavidin (VectorLabs, UK) were used at 1:250 and 1:500 dilutions respectively were used in a carrier solution containing 10% goat serum and PBS for a two-hour incubation at RT. Finally, the slices were washed thrice in PBS and transferred to 30% sucrose (Thermofisher, UK) until cryoprotected. Then slices were re-sectioned at 100-micron thickness using SM2010R freezing microtome (Leica, UK)) at -20°C and mounted onto glass-slides and HardSet mounting medium with DAPI was used (VectorLabs, UK).

Behavioural assessment

Animals

Following acclimatisation, they were singly housed in rat cages (previously washed and sterilised to eliminate any other species smells), equipped with a running wheel and two water bottles. One water bottle was filled with 0.1% (w/v) sucrose solution, available *ad libitum*, and mice were allowed to become familiar with the sucrose solution. Behavioural testing was conducted throughout (nest-building, sucrose preference) or on day 4, 24 hours after the last application of cream. Elevated plus maze was conducted in the morning and mice were returned to their cage room for 2 – 3 hours before performing open field test in the afternoon. Before each test, mice were allowed to acclimatise to the behaviour room for 30 mins prior to the start of testing.

Sucrose preference

Mice were allowed to establish their pattern of consumption of water and sucrose over the course of several days, prior to the treatment with topical creams. Both water bottles were weighed in the mornings and evenings and the change in weight was compared as a ratio of sucrose preference.

Nest building

We used the Deacon nest building protocol (*20*). Pressed unbleached cotton squares of 3 g (± 0.05 g) each were given every morning for nest building and collected the following morning. The images of the nests were taken for rating out of 5 (where 5 points were given to a fully shredded cotton material built up into a high walled nest, covering the mouse; 1 point reflects an untouched pressed cotton material) in the evenings as well as following mornings. The non-shredded material was weighed as another measure of nest building.

Elevated plus maze

To assess anxiety, mice were placed into cross shaped Perspex arena (110 cm x 110 cm, 65 cm from ground) for one trial of 5 mins only and recorded using ANY-maze video-tracking software (ANY-maze, Ireland). ANY-maze software was also used to analyse the following: distance travelled, average and maximal speed in different parts of the arena (closed arms *vs* open arms) as well as numbers of entries and time spent in open arms (OA) versus closed arms (CA) of the arena.

Open field test

To assess locomotor activity and get a secondary measure of anxiety in a novel arena environment, mice were placed into individual Perspex boxes (40 x 40 x 45 cm) for 1 h and recorded using ANY-maze video-tracking software. First 15 mins were analysed using ANY-maze software, and measures recorded included distance travelled, average and maximal speed in different parts of the arena as well as numbers of entry and time spent in centre and perimeter of the arena.

Rotarod

We measured locomotor activity using an ITC Rotarod (IITC Life Sciences Inc, USA). Mice were habituated to the room for 30 min prior to testing, and acclimatised to the accelerating rotarod (0 – 60 rpm) for 3 trial runs the day before recording. A baseline performance was recorded immediately before the first topical cream application. Mice were placed on the beam in separate lanes of the rotarod apparatus. Latency to fall from the rod was recorded for up to 300 s each trial for three trials per day on 3 consecutive days. The latency to fall compared to the baseline was reported per mouse and compared between groups.

Statistical analysis

Data were checked for normality using Shapiro-Wilk's test and parametric tests were used throughout, unless otherwise specified; outliers were tested for using ROUT test. No animals were excluded from the data analysis. Comparisons were made using either unpaired two-tailed t-test (e.g. For total average speed in EPM maze for control and Aldara-treated animals) or one-way ANOVA with multiple comparisons and Tukey correction. Data is presented as mean ± SD unless otherwise stated.

Results

Behavioural assessment of mice following 3 days Aldara treatment

We carried out behavioural testing to ascertain whether the neuroinflammation induced by topical application of Aldara cream over the course of 3 days induced changes in reward and motivation phenotypes and anxiety-like behaviour. We used the nest building assay (*20*) as a measure of intrinsic motivation in mice. Mice were provided with 3.0 g nestlet each evening and we measured the amount of unused nestlet the following morning. After 3 days of treatment, we observed a significant increase in the amount of unused nestlet in Aldara-treated mice relative to controls (1.1 ± 0.2 g *vs* 0.38 ± 0.1 g; $p = 0.0403$ in *post hoc* Šídák's multiple comparisons test after two-way ANOVA; Fig. 1A). Additionally, the quality rating of the nest built by the mice over the 24h period progressively

deteriorated in Aldara-treated mice, reaching significance at day 3 post-treatment (Fig. 1B). In contrast, control mice displayed a trend for a progressive improvement in nest quality. Examples of nests, corresponding to each of the possible grades for next building are shown in Supplementary Fig. 1. Overall, the nest building assay suggested a reduction in intrinsic motivation in Aldara-treated mice.

To further assay anhedonic-like behaviour, we used the sucrose preference test. We measured the sucrose-to-water ratio (weight change in sucrose solution divided by the weight change in water solution in the previous 12 hours) twice daily, to account for the nocturnal cycle of mice: their baseline preference for sucrose was absent during the daytime (typical ratio of 1 for both groups) but was on average ~4 during the night in both groups. Aldara treatment significantly reduced the preference for sucrose at night, relative to control-treated mice (Fig. 1C). Together, the nest-building assay and sucrose preference test both indicate an emerging anhedonia-like phenotype after 3 days treatment with Aldara.

We used the rotarod test to assess motor capability in evoked movement in Aldara-treated mice. There was no significant difference in rotarod performance (time to fall relative to baseline) between treatment groups ($p = 0.3186$, two-way ANOVA, Fig. 1D), demonstrating there were no motor impairment due to Aldara treatment. We sought to determine whether, in addition to an anhedonia-like phenotype, Aldara treatment also evoked anxiety-like behaviours. We used the elevated plus maze (EPM) as a primary measure of anxiety. Both groups of mice spent less time in open arms than the closed arms (example heat-maps in Fig. 1E), with Aldara-treated animals not spending a lower percentage of time in open arms than control-treated mice ($p = 0.2276$, unpaired two-tailed t-test, Fig. 1F). Interestingly, however, Aldara-treated mice spent a significantly longer period immobile ($p = 0.0093$, unpaired two-tailed t-test, Fig. 1G) relative to control mice. Additionally, these mice displayed a significantly greater number of immobile periods ($p = 0.0039$, unpaired two-tailed t-test, Fig. 1H) on the elevated plus maze than control mice, demonstrating a start-stop like activity within the test. Additional EPM data are presented in supplementary Fig. 1. Combining the EPM and

rotarod data, it appears that while Aldara treatment did not induce an anxiety-like phenotype and mice behaved normally when forced to move, there appeared to be a reduction in self-driven exploratory movement in the EPM. This observation further reinforces the conclusion that Aldara treatment drives anhedonic-like behaviour.

Open field test, carried out in the afternoon on the same day as EPM, Aldara-treated mice displayed no evidence of changes in locomotor activity relative to controls, measured as total distance travelled in the maze ($p = 0.5054$, Mann-Whitney test; Fig. 1J) or as total velocity in the maze ($p = 0.4242$, Mann-Whitney test; Fig 1K). Both groups exhibited a preference for the perimeter of the open field maze over the centre (Supplementary Fig. 1), but Aldara-treated mice did not display any difference in percentage of time spent in the centre (a proxy measure of anxiety) relative to controls ($p = 0.5198$, unpaired t test, Fig 1L). Unlike in EPM, the mice did not display significant reductions in self-driven movement in the open field test. This may be due to EPM being carried out first in the morning (immediately after mice had finished their active period) but mice subsequently having had ~5 hours of sleep by the start of open field testing.

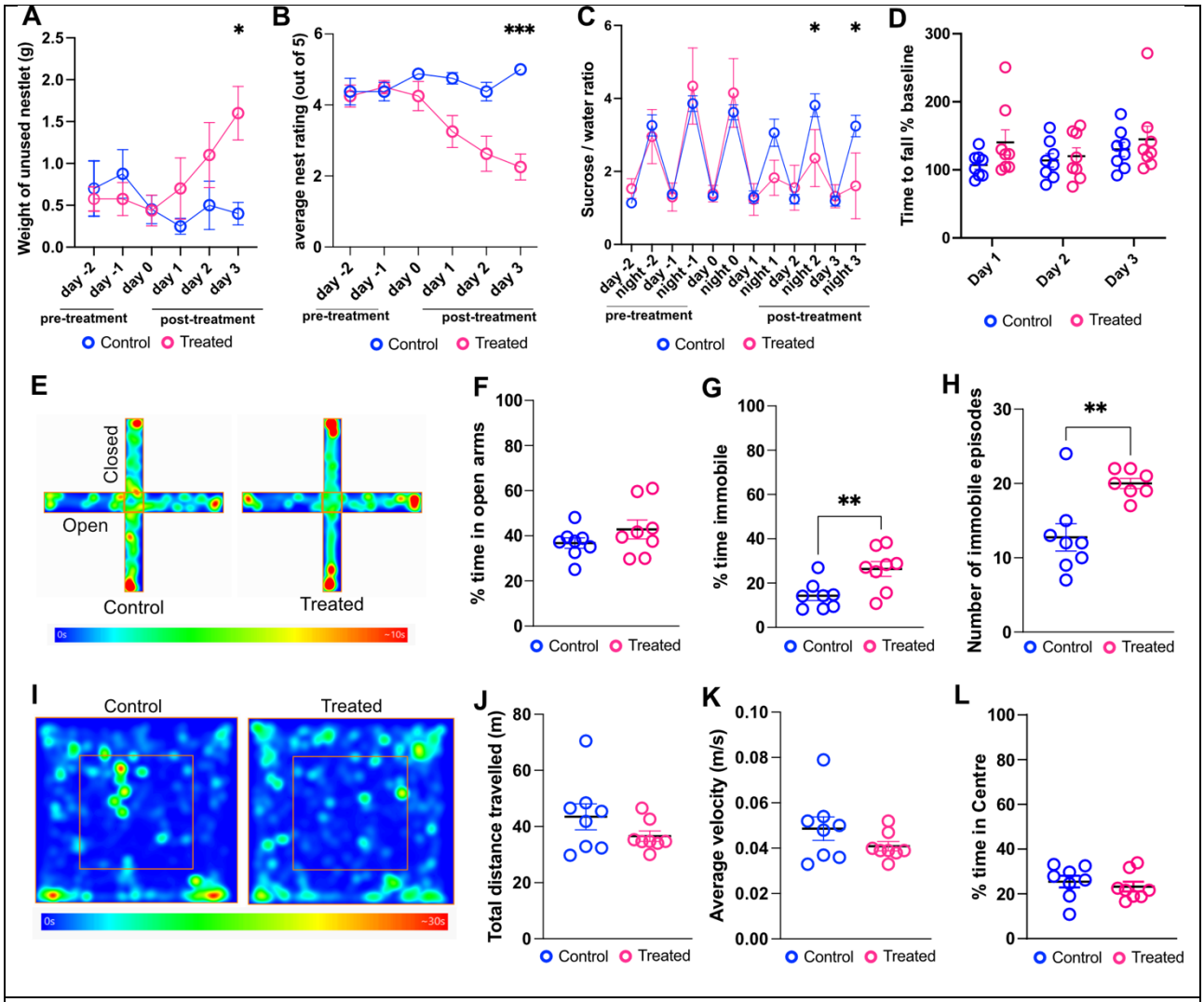

Figure 1: Behavioural assessment of 3-day Aldara-treated mice. In all panels control mice are shown in blue and Aldara-treated mice in pink. **A**, Nest-building assay across treatment time: significant interaction between Aldara treatment and time on amount of unused nestlet (p=0.0079, two-way ANOVA with Šídák's *post hoc* test). **B**, Aldara treatment caused increasingly lower nest-building ratings across time which reached significant on day 3 (Effect of treatment: p = 0.0007; effect of time: 0.0067; interaction: p < 0.0001; Two-way ANOVA with Šídák's *post hoc* tests; 5 is highest and 1 is lowest). **C**, Sucrose preference at day and night during treatment. Significant interaction between treatment and time (p < 0.0001; Two-way ANOVA) with Aldara-treated mice showing significantly less preference for sucrose during the night after 2 and 3 days of treatment (Šídák's *post hoc* tests). **D**, Rotarod performance (% time to fall from the rod compared to baseline) was evaluated every day prior to cream treatment. **E**, Representative heatmaps from elevated plus maze (EPM) recordings performed 24h following final treatment. **F**, Percentage time spent in open arms compared to closed arms of the EPM. **G**, Time immobile (immobility defined as not moving for longer than 2 seconds) in 5-minute trial. **H**, total number of immobile episodes during EPM testing. **I**, representative examples heatmaps of open field (OF) exploration for control and Aldara-treated mice. **J**, total distance travelled during OF testing. **K**, average velocity of mice during OF testing. **L**, Percentage time spent in the centre of OF maze. Scatter plots display data points (each point is one animal) and mean + S.E.M; n=8 mice per group in all tests; *, p < 0.05; **p < 0.01; *** p < 0.005.

Transcriptional changes associated with neuroinflammation

Previously, we described neural transcriptional changes within the Aldara model using selected qPCR methods (*11*). We sought to expand on this in an unbiased manner, so deployed whole-brain transcriptomic analysis using RNAseq. We extracted RNA from brains of mice that had undergone Aldara treatment and those receiving the control cream (n=5 mice per group). A principal component analysis (PCA) revealed that the pattern of gene expression was significantly different between the two groups (Fig. 2A). A differential expression analysis using DESeq2 (*14*) revealed that, relative to control mice, there were 2198 significantly upregulated and 585 significantly downregulated genes in the brains of Aldara-treated mice (Fig. 2B). To control over representation of very highly expressed genes, all gene expression values were scaled on a gene-by-gene basis using the Z-score transformation, prior to the PCA being run.

We next carried out an overrepresentation analysis (ORA) using G:Profiler (*16*) to determine the biological functions of the genes and their pathways that were differentially expressed in response to Aldara treatment. We first ran the ORA using the KEGG (*21*), Reactome (*22*) and WikiPathways (*23*) databases to understand the broad function of upregulated and downregulated gene sets. Manhattan plots for the ORA for upregulated and downregulated gene sets are shown in Fig. 2C and Fig 2D, respectively. There is substantial overlap in function between different gene sets, so we have highlighted pathways in Fig. 2C – D that were of greatest biological relevance; the full datasets are included as supplementary files. Among the upregulated pathways, immune activation-related pathways are observed including immune cell (T cell, B cell, NK cell and macrophages) activation, anti-viral and inflammatory responses, cytokine, chemokine and toll-like receptor signalling pathways and those related to microglial activation (Fig. 2C). With TLR7/8 activation being the basis of the Aldara model, these immune-related pathways can be expected to have an upregulated biology and present transcriptional basis for follow-up molecular and cellular work presented in this current study. There were fewer significantly downregulated pathways but those that we detected were related to glutamate metabolism, neurotransmitter release, glutamatergic synapses and purinergic receptor signalling (Fig. 2D). These changes are broadly indicative of disrupted glutamatergic signalling. We

carried out a second ORA using the Gene Ontology: Biological Processes database (*24*) for upregulated and downregulated genes. This search produced many more hits than the pathways databases, but the relevant biological functions broadly agreed with those using the former analysis. Manhattan plots and highlighted genes are shown in Supplementary Fig. 2, and the full datasets are included.

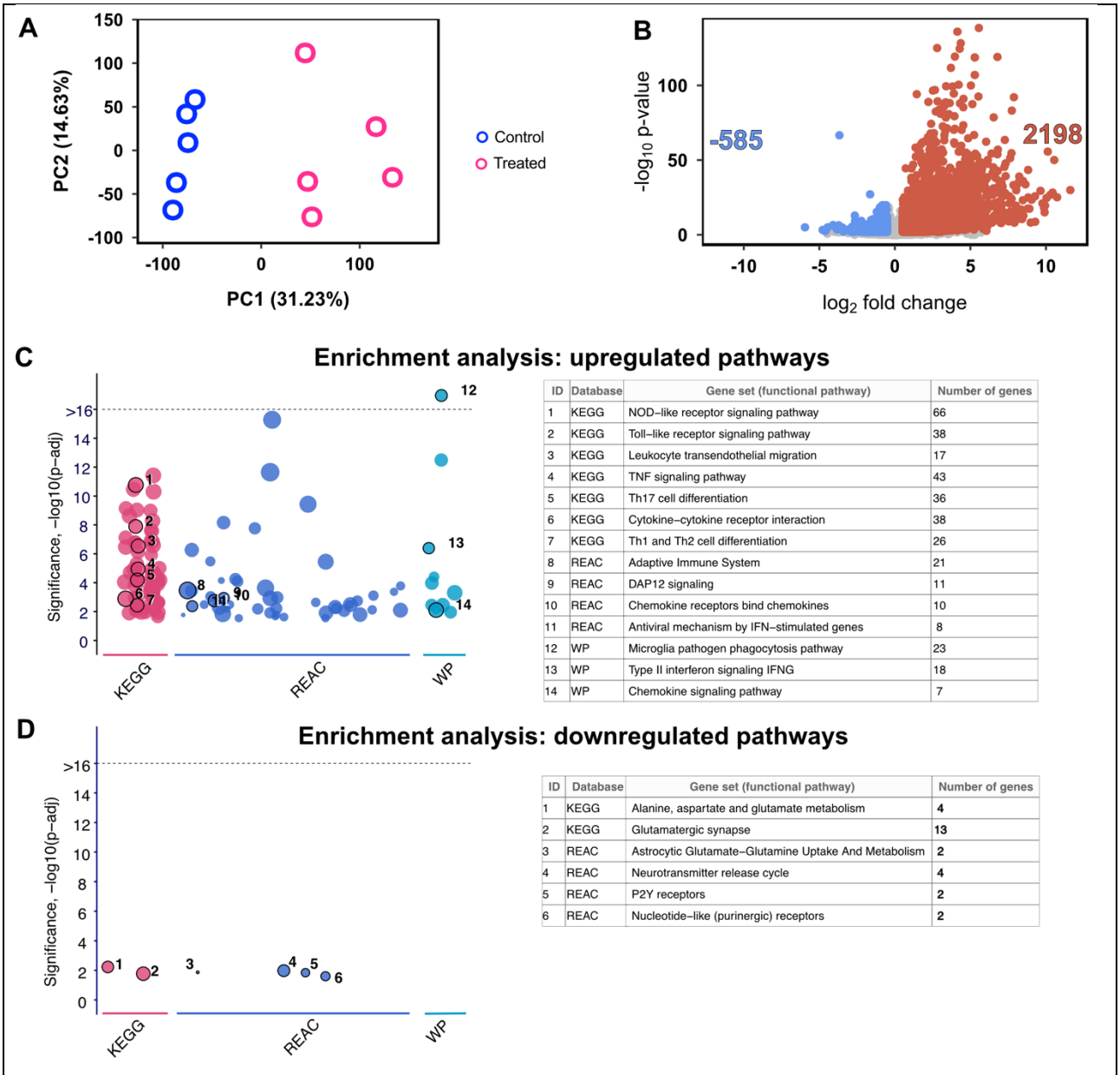

ID	Database	Gene set (functional pathway)	Number of genes
1	KEGG	NOD−like receptor signaling pathway	66
2	KEGG	Toll−like receptor signaling pathway	38
3	KEGG	Leukocyte transendothelial migration	17
4	KEGG	TNF signaling pathway	43
5	KEGG	Th17 cell differentiation	36
6	KEGG	Cytokine−cytokine receptor interaction	38
7	KEGG	Th1 and Th2 cell differentiation	26
8	REAC	Adaptive Immune System	21
9	REAC	DAP12 signaling	11
10	REAC	Chemokine receptors bind chemokines	10
11	REAC	Antiviral mechanism by IFN−stimulated genes	8
12	WP	Microglia pathogen phagocytosis pathway	23
13	WP	Type II interferon signaling IFNG	18
14	WP	Chemokine signaling pathway	7

ID	Database	Gene set (functional pathway)	Number of genes
1	KEGG	Alanine, aspartate and glutamate metabolism	4
2	KEGG	Glutamatergic synapse	13
3	REAC	Astrocytic Glutamate−Glutamine Uptake And Metabolism	2
4	REAC	Neurotransmitter release cycle	4
5	REAC	P2Y receptors	2
6	REAC	Nucleotide−like (purinergic) receptors	2

Figure 2: Whole-brain transcriptome changes due to Aldara treatment. **A**, Gene expression data principal component analysis (PCA) scatterplots with each point representing an animal. The percentage of total variation explained by each component is given in the X and Y-axis as appropriate. **B,** Volcano plot for differential expression analysis of Aldara treated samples relative to controls. Significantly differentially-expressed genes (p value adjusted <0.05, absolute $\log_2$ fold > 0.5) are shown in red (up-regulated) and blue (down-regulated), with non-significant genes in grey. **C & D**, Manhattan plots showing enriched pathways in overrepresentation analysis for upregulated (**C**) and downregulated (**D**) genes. ORA carried out using KEGG, Reactome and WikiPathways databases.

Immune cell infiltration into the brain following Aldara treatment

We have previously shown that 3 days of treatment with Aldara is sufficient to trigger an ingress of immune cells into the brain (*11*). We carried out flow cytometry and immunohistochemistry experiments to allow us to determine which immune cell type(s) were entering the brain, with these data summarised in Fig. 3, and our gating strategies for all following flow cytometry experiments provided in supplementary materials. Flow cytometry of brain single cell homogenates showed expression of 4 key populations based on two classical makers CD45 and CD11b (Fig. 3A). The four cell populations were: non-immune ($CD45^{-}CD11b^{-}$); lymphoid ($CD45^{+}CD11b^{-}$); myeloid ($CD45^{hi}CD11b^{+}$); and microglia ($CD45^{int}CD11b^{+}$), as previously defined by others (*25*).

Aldara treatment caused a substantial increase in lymphoid and myeloid cells in brain homogenates (Fig. 3A) and we observed an overall increase in the number of cells present in the homogenate (Fig. 3B) relative to controls. This increase was due to the immune cells ($CD45^{+}$) forming a significantly larger percent of the total brain cell homogenate population after Aldara treatment when compared to controls (37.6 ± 3.1% *vs* 7.1 ± 1.0%, n=36 mice per group; $p < 0.0001$, unpaired t test with Welch's correction; Fig. 3C). Of the immune cells infiltrating the brain due to Aldara treatment, this population was primarily comprised of significantly increased numbers of monocytes, B cells, NK, and NKT cells (Fig. 3D; note that data are plotted on a logarithmic scale).

Flow cytometry showed an increase in the number of $CD3^{+}$ T cells in the brain after Aldara treatment (Fig. 3E) and, of these, we saw significantly increased level of $CD4^{+}$ and $CD8^{+}$ T cells (Fig. 3E – F). Regionality of infiltrating T cells was assessed using immunohistochemistry. We found a uniform increase in $CD4^{+}$ cells in all brain regions tested (Fig. 3G – 3H), although the density of $CD4^{+}$ T cells did not reach significance on *post hoc* multiple comparisons tests for hippocampus and ventral striatum (Fig. 3H). Overall, both flow cytometry and immunohistochemistry confirm that Aldara treatment is associated with substantial peripheral immune cell ingress into the brain, with an apparently uniform brain parenchymal penetration.

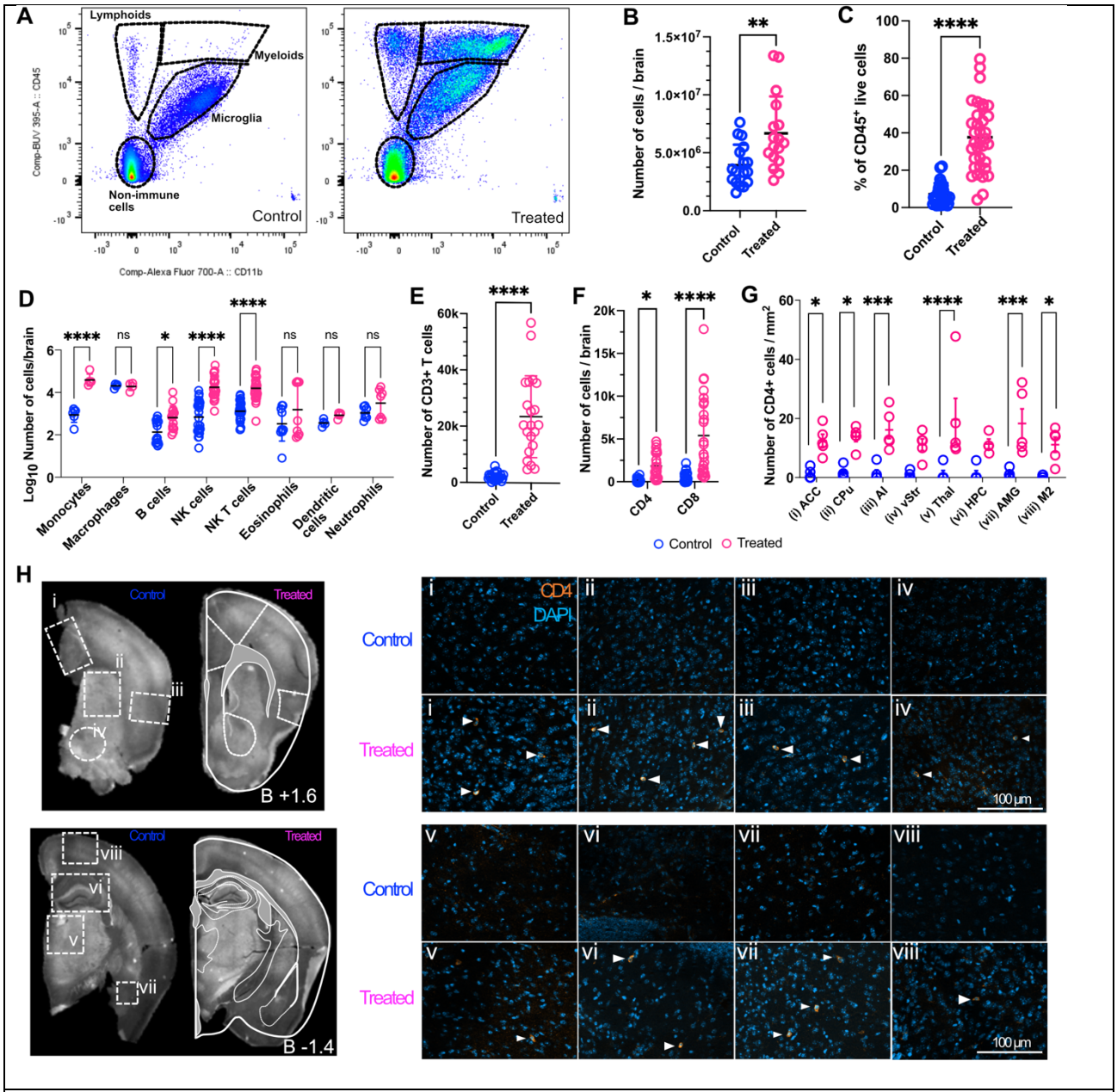

Figure 3: Ingress of peripheral immune cells into the brain is observed after 3 days of Aldara treatment. In all panels, control mice are shown in blue and Aldara-treated mice in pink. **A,** Representative basic flow cytometry panels from a single control (left) and Aldara-treated (right) brain. The 4 broad cell types are indicated within dashed lines. **B,** total number of cells found in the brain homogenates from control- and Aldara-treated mice. **C,** relative proportion of live CD45+ cells in control- and Aldara-treated brain homogenates. **D,** numbers of different immune cell types, as measured with flow cytometry, in control- and Aldara-treated brain homogenates (data plotted on log scale). **E,** absolute numbers of CD3-expressing T-cells in control and Aldara-treated mice. **F,** Aldara treatment led to a significant increase in the numbers of CD4- and CD8–expressing T-cells. **G,** Summary immunohistochemistry data for density of CD4+ T cells in multiple brain regions. **H,** Representative example of coronal slices taken from anterior (Bregma +1.6, left) and posterior (Bregma -1.4, right) brains. Brain regions for CD4+ quantification are highlighted: **i**, anterior cingulate cortex (ACC); **ii**, caudate putamen/dorsal striatum (CPu); **iii**, agranular insular cortex (AI); **iv**, nucleus accumbens/ventral striatum (vStr); **v**, midline thalamus (thal); **vi**, dorsal hippocampus (HPC); **vii**, amygdala (AMG); **viii**, motor cortex (M2). Representative images of each region from control and Aldara-treated brain sections are shown (CD4 orange, DAPI blue), positive cells are indicated by white arrowheads. Scale = 100 µm. Each point represents an individual animal (4 animals per experiment and cumulative at least 4 – 5 experiments per flow result), mean

± S.E.M. Unpaired t-tests (with or without Welsch's correction as appropriate) were carried out on data from B, C, E, F; two-way ANOVAs were carried out on data on D and G. *, $p < 0.05$; **, $p < 0.01$; ***, $p < 0.005$; ****, $p < 0.0001$.

Alterations in glial cells following Aldara treatment

To ascertain whether Aldara drove changes in astrocytes and microglia, we performed flow cytometry and immunostaining. Given that peripheral inflammation can drive microglial activation (reviewed by *26*) used IBA-1 showing that, qualitatively, microglial morphology significantly changed after Aldara treatment, becoming less ramified with larger, more ameboid-like cell bodies compared to controls, indicative of activation (Fig. 4A). However, there were no significant quantitative changes in IBA-1 average intensity (Fig. 4B) or total area covered by IBA-1 (Fig. 4C), with hippocampus being the only region showing a significant change. Flow cytometry gating with $CD45^{int}$ and $CD11b^{hi}$ for microglia showed increases in Aldara treated compared to control mice (Fig 4D). Similarly, activated microglia markers, MSR1 (Fig. 4E), F4/80 (Fig. 4F) and MHCII (Fig. 4G) all confirmed the increased number of activated microglia in Aldara-treated mice. Transcriptomic analysis confirmed that several genes associated with microglial activation were upregulated in Aldara-treated mice (Supplementary Fig. 3A).

Conversely, immunohistochemistry staining with GFAP did not show major changes in astrocyte immunoreactivity or morphology in response to Aldara treatment (Fig. 4H), nor were there changes in average GFAP intensity (Fig. 4I) or area covered (Fig. 4J). GFAP (Fig. 4K), S100β (Fig. 4L) and ACSA2 (Fig. 4M) were used as markers to identify potential astrocytic activation in flow cytometry, but we found little evidence in differences in the individual expression profile of these three markers in the treated brains compared to control. However, there was significant increase in the triple positive astrocytes for GFAP, S100β and ACSA2 (Fig. 4N) in the Aldara treated mouse brains, which could provide putative evidence of activation. Transcriptomic analysis also found upregulation of genes associated with astrocytic activation in Aldara-treated mice (Supplementary Fig. 3B). In summary, there is evidence of activation of two key neural cell populations, both of which are potential sources of inflammatory cytokines.

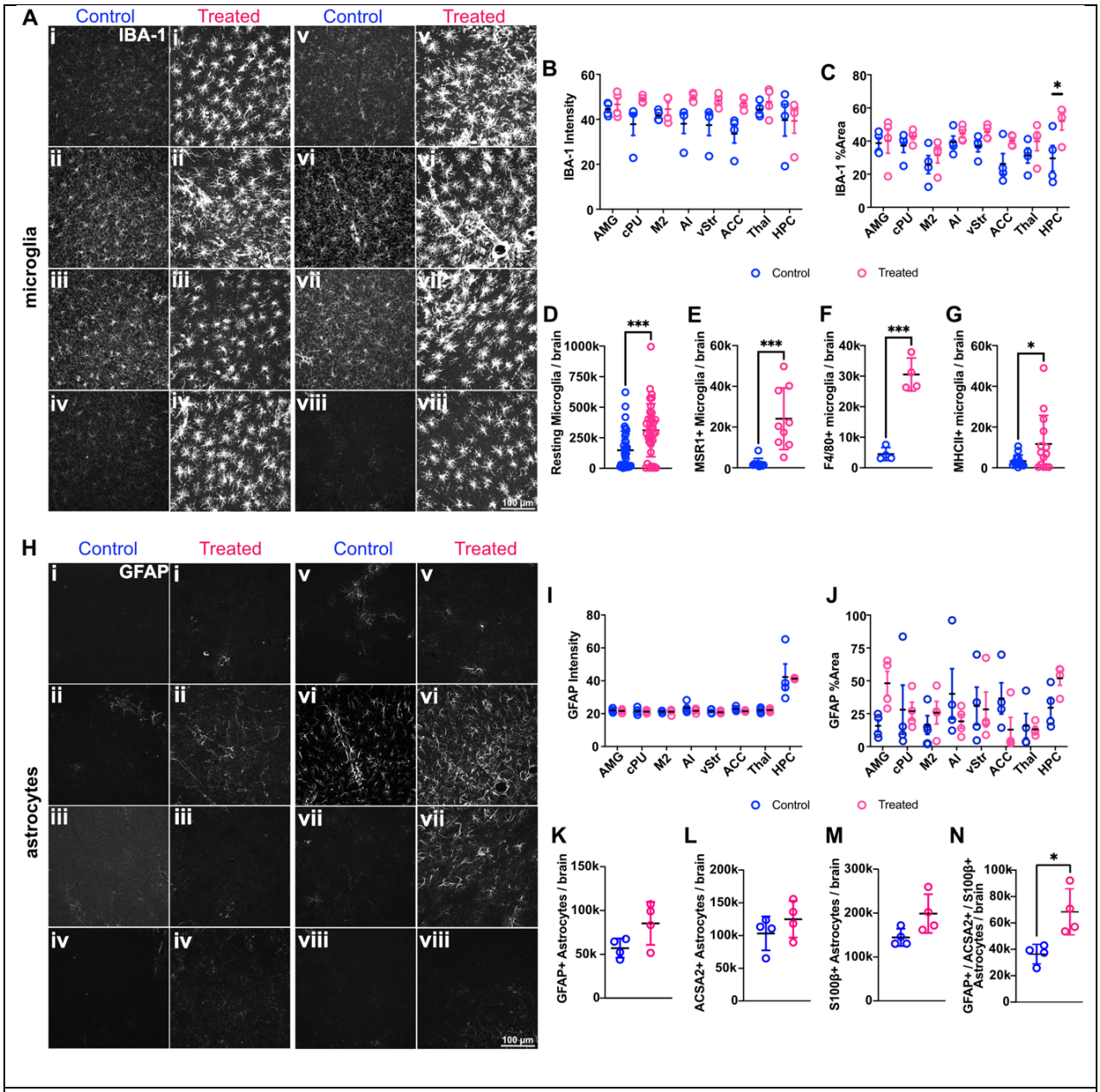

Figure 4: Alterations in microglia and astrocytes following Aldara treatment. In all panels control mice are shown in blue and Aldara-treated mice in pink. **A**, images taken from immunohistochemistry stain for IBA1 in control- and Aldara-treated brains for: **i**, anterior cingulate cortex (ACC); **ii**, caudate putamen/dorsal striatum (CPu); **iii**, agranular insular cortex (AI); **iv**, nucleus accumbens/ventral striatum (vStr); **v**, midline thalamus (thal); **vi**, dorsal hippocampus (HPC); **vii**, amygdala (AMG); **viii**, motor cortex (M2). **B**, average density of IBA1 stain (on an 8-bit scale, so 0 to 255) for control- and Aldara-treated brains. **C**, total % area of section labelled for IBA1 for same samples. **D – G**, flow cytometry counts for total number of cells in brain homogenate from control- and Aldara-treated mice, selecting for the following microglia markers: total microglia (CD45int and CD11bhi; **D**), MSR1 (**E**), F4/80 (**F**), MCHII (**G**). **H,** images taken from immunohistochemistry stain for GFAP in control- and Aldara-treated brains for same regions as **A**. **I**, average density of GFAP stain (on an 8-bit scale, so 0 to 255) for control- and Aldara-treated brains. **J**, total % area of section labelled for GFAP for same samples. **K – N**, flow cytometry counts for total number of cells in brain homogenate from control- and Aldara-treated mice, selecting for the following astrocyte markers: GFAP (**K**), ACSA2 (**L**), S100β (**M**), GFAP / ACSA2 / S100β triple positives (**N**). *, p <0 .05; ***, p < 0.005.

Cellular inflammatory response following Aldara treatment

To determine if Aldara treatment altered the inflammatory response of both infiltrating peripheral immune cells and brain-resident cells, we used both flow cytometry and further analysis of the whole brain transcriptome dataset. There were significant increases in different subsets of infiltrating $CD4^+$ and $CD8^+$ T cells in brain parenchyma in treated mice, with increases in Th1 cells secreting TNFα, T (IL-4) and Th17 cells secreting IL-17, but no significant differences in Th2 cells secreting the anti-inflammatory IL-4 (Fig. 5A – C, respectively). These data indicate a Th1/Th17 signature of T cells in brain in this model of neuroinflammation.

We also directly assayed for expression of proinflammatory cytokines (TNFα, IL-6 and IFN-γ) in microglia and astrocytes, Aldara treatment caused a significant increase in the number of microglia producing all 3 cytokines relative to controls (Fig. 5E), as well as significantly increasing the number of astrocytes that were producing IL-6 and IFN-γ (Fig 5F). Finally, we also observed a significantly increased proinflammatory signature of infiltrating monocytes (producing TNFα and IL-6) in the treated mice (Fig. 5G). Our gating strategies for the flow cytometry experiments are presented in the supplementary material.

We interrogated the whole brain RNAseq dataset for expression of a range of chemokines, cytokines and their receptors (Fig. 5D). As shown in the heatmap, the whole brain inflammatory profile broadly corresponded with the flow cytometry data and the overall trend was for upregulation of a wide range of both cytokines and chemokines. It should be noted that the flow cytometry experiment measured specific cytokines in specific cell types, while the transcriptomic data covers total gene expression across all cells in the brain, both resident and infiltrating. The complete transcriptomic data can be found in supplementary methods. Overall, these data show a widespread cellular inflammatory response as a result of Aldara-driven neuroinflammation.

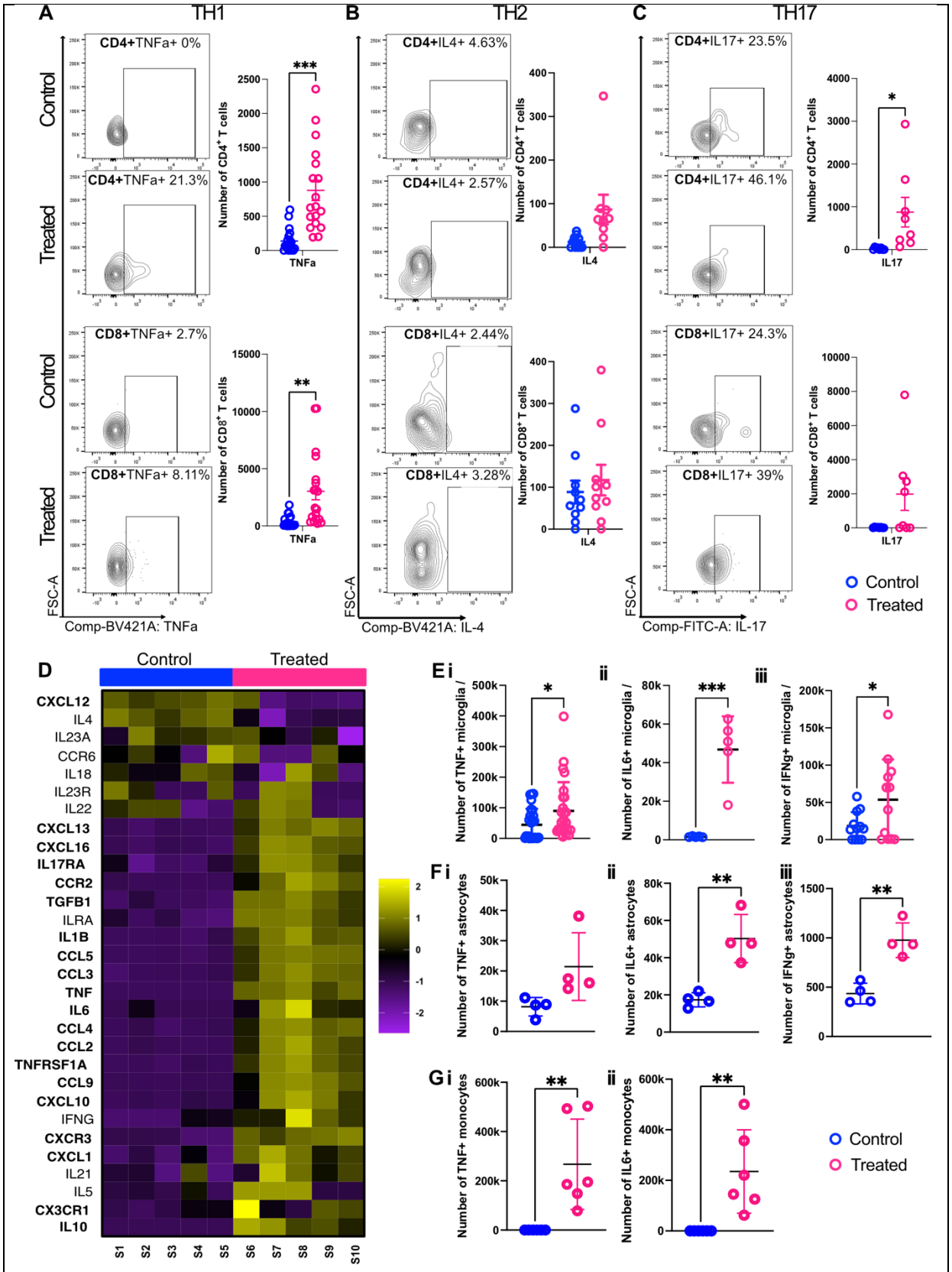

Figure 5: Aldara induces a neuroinflammatory response via multiple cell types. In all panels control mice are shown in blue and Aldara-treated mice in pink. **A – C,** Contour maps showing the numbers of CD4$^+$ (upper two) and CD8$^+$ (lower two) T cells in brain homogenates from control- and Aldara-treated mice. **A**, Expression of Th1 type cytokine TNFα increases in Aldara-treated brains. **B,** No change in IL4, a Th2-type cytokine, was observed in response to Aldara treatment. **C**, Aldara treatment resulted in an increase in IL-17 expression in CD4$^+$ but

not $CD8^+$ T cells. **D**, Searchlight heatmap showing relative expression levels for a range of cytokines from control- and Aldara-treated mice. Each square on the heatmap represents one mouse. **E – G,** flow cytometry data measuring cytokine expression in microglia (**E**), astrocytes (**F**) and infiltrating peripheral myeloid cells (**G**). Microglia and myeloid cells, but not astrocytes, displayed a significant increase in TNFα expression (**i**), all cell types had a significant increase in IL-6 expression (**ii**), and both astrocytes and microglia increased expression of IFN-γ (**iii**). Each data point on flow cytometry plots represents a single animal. Data plotted as mean ± S.E.M. Unpaired two-tailed t-tests were performed on data comparing control and treated animals; *, $p < 0.05$; **, $p < 0.01$; ***, $p < 0.005$.

Neuroinflammation drives functional changes in thalamostriatal circuitry

Given the observed anhedonic phenotype (Fig. 1), we examined neural activity using immunohistochemistry for the immediate early gene product Fos, an established marker of neuronal activity, 4 hours after treatment with Aldara. This time point was chosen as we had previously shown via mass spectrometry that Aldara enters the brain within this time period (*27*). We found evidence of a significant increase in activity of midline thalamus of Aldara-treated mice relative to controls (Fos-reactive cells / mm^2, control *vs* treated: 25 ± 11 x *vs* 353 ± 32 y, $p < 0.0007$; unpaired Student's *t* test; Fig 6A).

Being guided by these data and the evidence for disrupted cortico-thalamo-striatal circuity in psychiatric phenotypes (29), we carried out stereotaxic surgeries to deliver AAV vectors to transduce expression of the excitatory opsin Chronos-GFP (*28*) to neurons in midline thalamus, with an injection site targeting the border of PVT and CM (Fig 6C & D). As expected, this led to widespread expression of Chronos-GFP in thalamic axons spread throughout ventral striatal regions including nucleus accumbens (Fig 6E & F). We made patch-clamp recordings from medium spiny neurons (MSNs) in ventral striatum, confirmed with *post hoc* morphological recovery (Fig 6G). We found a large and significant reduction in the AMPA receptor-mediated component of the midline thalamic EPSC onto ventral MSNs in Aldara-treated mice relative to controls (AMPA EPSC magnitude, control (n=11 neurons) *vs* treated (n=14 neurons): 225 ± 72 pA *vs* 57 ± 16 pA; $p = 0.0038$, Mann-Whitney test; Fig 6H & J). However, we found no statistically-significant reduction in the NMDA receptor-mediated component of the EPSC (NMDA EPSC magnitude, control (n=8 neurons) *vs* Aldara (n=7 neurons): 143 ± 32 pA *vs* 53 ± 20 pA; $p = 0.0541$, Mann-Whitney test; Fig 6H & K). While the statistical test did not reach the threshold for significance, the data appeared to be trending towards

a reduction in Aldara treatment, with the lack of significance likely due to a lower sample size available for this part of the study. Indeed, we saw no significant change in the ratio of AMPA/NMDA currents due to Aldara treatment, supporting the conclusion that both glutamatergic currents were reduced (AMPA/NMDA ratio, control (n=8) *vs* treated (n=7): 2.5 ± 0.7 *vs* 1.8 ± 0.5; p = 0.6126, Mann-Whitney test; Fig 6L).

To test whether the neuroinflammation-driven change in thalamic EPSC may be due to altered presynaptic release, we examined spontaneous EPSCs of ventral MSNs. We found no significant effect of Aldara treatment on either the amplitude (sEPSC amplitude, control (n=17) *vs* treated (n=25): 10.4 ± 0.6 pA *vs* 11.9 ± 0.6 pA; p = 0.1014, Mann-Whitney test; Fig 6I & M) or frequency (sEPSC frequency, control *vs* treated: 3.4 ± 0.5 Hz ± 3.5 ± 0.8 Hz; p = 0.6481, Mann-Whitney test; Fig 6I & N) of sEPSCs. Finally, we found that treatment with Aldara did not significantly alter the input resistance of MSNs (input resistance, control (n=17) *vs* treated (n=26): 65.2 ± 6.3 MΩ *vs* 62.5 ± 6.2 MΩ; p = 0.4057, Mann-Whitney test).

We further interrogated our whole brain transcriptome dataset to gain insights into the potential mechanisms that may be underlying the impairment in the thalamostriatal EPSC. The ORA revealed a significant downregulation in pathways associated with glutamatergic synapses, neurotransmitter release and glutamate metabolism (Fig. 2C). We also examined the expression of selected individual genes, covering a range of neurotransmitter receptor subunits, synthesis and metabolism, and neurotransmitter transporters (Fig. 6B). There was a general trend of downregulation in the majority of these gene sets, with significant downregulation of genes encoding GluN1 and GluN2C subunits of the NMDA receptor. There were no significant changes in AMPA, kainate or dopamine receptor subunit expression. Interestingly, both *Homer1* and *Homer2* were significantly downregulated on a brain-wide basis, implying disruption to maintenance of glutamatergic synapses (*29*). Genes involves in glutamate synthesis and metabolism, *Glul* and *Gls* were significantly downregulated. Of the amino acid transporters, only the astrocyte-specific EAA2 (encoded by *Slc1a2*) was significantly downregulated, implying an impairment in astrocytic glutamate reuptake. We also saw significant

downregulation of the dopamine transporter DAT (encoded by *SLC6A3*) and tyrosine hydroxylase, implying potential disruption of dopaminergic reward circuitry.

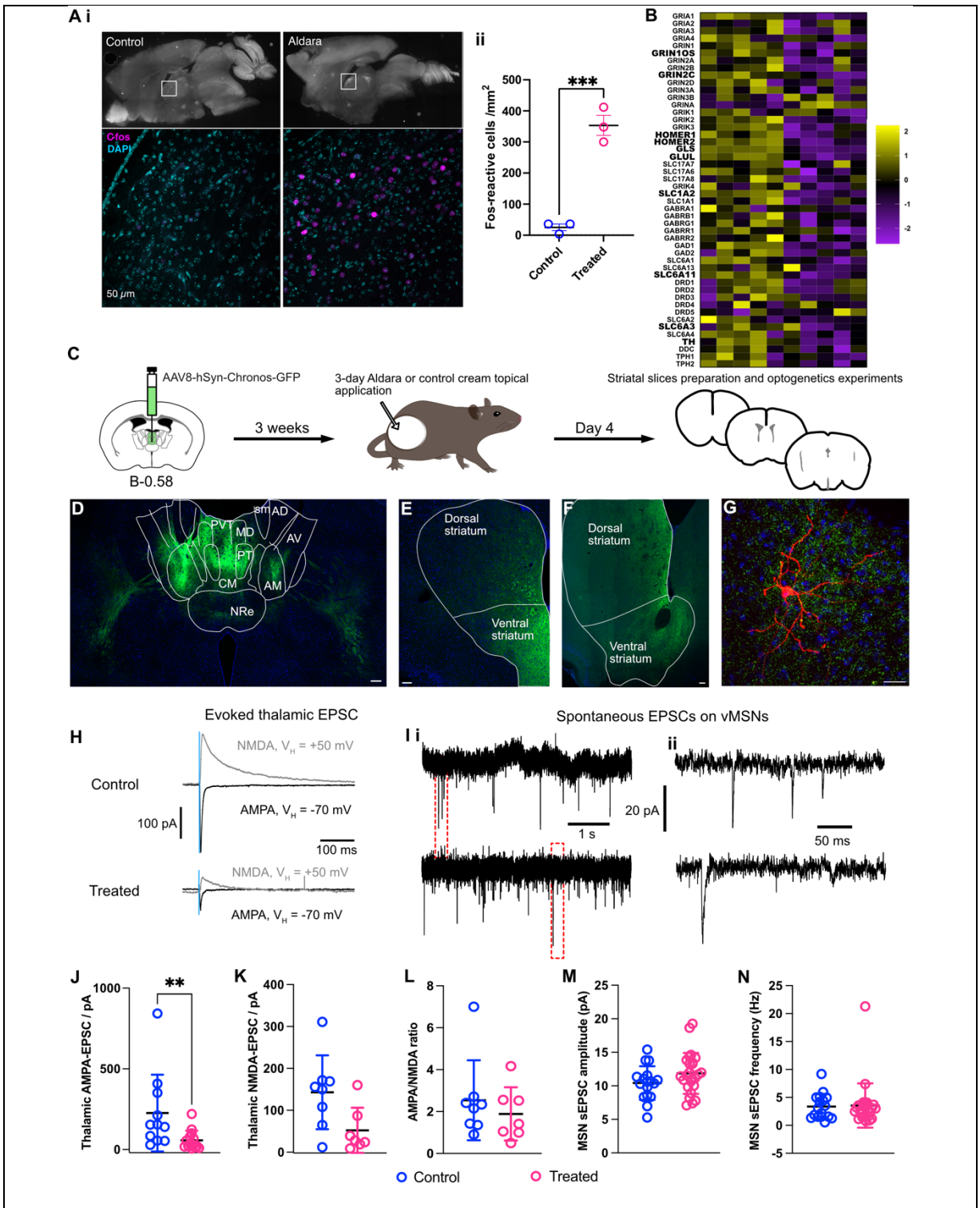

Figure 6: Aldara treatment drives functional changes in thalamostriatal network. A, significant increase in Fos-reactive nuclei in midline thalamus 4 hours after Aldara treatment. **B**, changes in expression for selected neurotransmission-related genes in bulk RNAseq samples after 3 days of Aldara treatment. Significant differences shown in bold. Scale bar indicates direction of change. **C**, schematic of experimental design for optogenetic and *ex vivo* patch clamp electrophysiology experiments investigating effect of Aldara treatment on midline thalamus projections to ventral MSNs. **D,** representative image of midline thalamus

showing expression of AAV8-hSyn-Chronos-GFP vector 3 weeks after injection. **E & F**, expression of thalamic fibres in rostral and caudal portions of striatum, respectively. **G**, post-hoc recovery of biocytin-filled MSN in ventral striatum (red) with thalamic axons expressing Chronos-GFP (green); DAPI stain in blue. **H**, representative traces of voltage-clamp electrophysiological recordings showing AMPA and NMDA receptor-mediated components of the optogenetics-evoked midline thalamic EPSC onto MSNs in the ventral striatum for control (top) and Aldara-treated (bottom) mice. **I**, spontaneous EPSCs on ventral MSNs for control (top) and Aldara-treated mice (bottom) recorded in voltage clamp mode (V_H = -70 mV). Red hatched area in **i** shown in **ii** on an expanded time base. **J**, Aldara treatment caused a significant reduction in the AMPA-receptor mediated thalamic EPSC but **K,** had no statistically significant effect on the NMDA-receptor mediated component. **L,** Aldara treatment had no significant effect on the AMPA/NMDA ratio of the thalamic input into ventral MSNs. **M & N**, Aldara treatment had no effect on the amplitude or frequency, respectively, of sEPSCs in ventral MSNs. *Abbreviations: AD, anterodorsal thalamus; AM, anteromedial thalamus; AV, anteroventral thalamus; CM, centromedial thalamus; MD, mediodorsal thalamus; NRe, nucleus reuniens; PVT, paraventricular thalamic nucleus.* All data taken from at least 4 mice per group (6 mice for eEPSC data) across 3 different litters, with only 1 neuron taken per brain slice.

Discussion

In this study, we sought to better understand the link between neuroinflammation and depression-like behaviours. Three consecutive days of treatment with TLR7 agonist (IMQ) Aldara resulted in neuroinflammation that evoked behavioural changes including reduced sucrose preference and impaired nest-building; these behaviours are consistent with an anhedonia-like state in mice (see e.g., *30* for a review of rodent anhedonia models). We employed a multi-scale approach to characterise the neurobiological changes occurring due to Aldara-driven neuroinflammation at the transcriptome, protein, cellular and synaptic levels. This neuroinflammation was associated with robust changes in gene expression, immune activation, infiltration of immune cells into the brain, including CD4+ T cells into the brain parenchyma, and a substantial reduction in midline thalamus-driven excitation of medial spiny neurons in the ventral striatum.

Behavioural changes in response to Aldara

We predicted that neuroinflammation would evoke a depression-like behavioural phenotype, including reduced motivation or anhedonia, as well as anxiety-like behaviours. While mice did indeed show reduced anhedonic-like behaviours via impaired nestbuilding and reduced sucrose preference, we found no evidence that Aldara treatment increased anxiety in either EPM or the open field test. Mice appeared to have normal locomotor function in open field and rotarod tests but displayed a

‘stop-start’ behaviour during EPM, which is tempting to speculate as showing a reduced intrinsic motivation to carry out exploratory behaviours. Our data fit with the existing literature that show other forms or neuroinflammation can evoke depression-like behaviours (*7*, *31*) and adds to the construct validity of Aldara as a model for inflammation-induced depression that is observed in humans (*4*, *5*). Treatment with Aldara evoked anhedonia-like behaviours without any apparent anxiety, which supports the assumption that these two symptoms of depression are driven by distinct changes in neural circuitry. Indeed, while anxiety and depression are often comorbid, with anxiety occurring in more than 40% of individuals with major depressive disorder, and depression occurring in around 50% of anxiety disorders (reviewed by *32*), these are distinct conditions. The Aldara model potentially offers a preclinical approach for separating reward/motivation from anxiety to allow a parsing of mechanisms underlying these behavioural phenotypes.

Transcriptional changes in response to Aldara

Bulk RNA sequencing of brain tissue provided an unbiased measure of the transcriptional response to Aldara. There were marked differences between Aldara brains and those of the controls. Among the most enriched pathways for upregulated gene sets were the innate immune response, type II interferon response, chemokine and TLR signalling pathway which concurs with our previous data on Aldara brain responses (*11*, *33*). Transcriptomic changes also revealed altered expression of cytokines and chemokines in Aldara-treated mice, relative to controls, that were consistent with a proinflammatory response. For example, TNF, IL6, IL1β and IFNγ were all upregulated. These data replicate those that we have previously reported (*11*, *27*, *33*). We found an upregulation of chemokines signalling pathways which highlight chemokines as being potential drivers of immune cell recruitment during neuroinflammation. Immune system gene expression was confirmed by upregulation of B cells, T cells, Monocytes, NK and NKT cells via flow cytometry (Fig 3). T cell signature pathways were also upregulated at transcriptional level, and we show a distinct T cell biology in our model. Several key microglial activation pathways were among the most upregulated including: Microglia phagocytic pathway, DAP12, which along with TREM2 is the principal regulator transforming microglia to a neural disease associated state and regulates microglial cytokine

production(*34*). Tyrobp is expressed on microglia and serves as an adaptor for immune receptors including TREM2 and a gene shown to be robustly upregulated in early transition of microglia from homeostatic to disease associated state (*35*). We see an activated microglial profile in this model of neuroinflammation.

The most enriched pathways for downregulated genes were those related to glutamate metabolism and neurotransmission, which was consistent with our electrophysiological findings of impaired thalamostriatal signalling (discussed further below). We also saw significant downregulation of the dopamine transporter and tyrosine hydroxylase; while we did not assay dopaminergic signalling in the present study, this could present an interesting future avenue of research. Overall, these transcriptional changes indicate a clear neuroinflammatory response focused on IFN-γ and TNFα as well as an immune cell response, notably T cell, to the Aldara stimulus. For both down- and upregulated gene pathways, data from the transcriptomic data were very complementary to those arising subsequent neurobiological and immunological experiments.

Immune cell infiltration, changes in brain-resident cells and their cellular responses

We found substantial immune cell infiltration of the brain after three days of Aldara treatment. Overall, there was a significant ingress of both lymphoid and myeloid cell types into brain. The upregulation in chemokine transcription noted above includes myeloid cell attractants (CCL2, CCL3 and CCL5) and lymphoid cell attractants (CXCL9, CXCL10 and CXCL16; Fig. 5D). Classically, these chemokines are the drivers of immune cells so it is possible that the ingress of immune cells could be, at least in part, due to upregulation of these chemokines.

Flow cytometry revealed the presence of $CD4^+$ T cells in the brains of Aldara-treated mice, with IHC confirming infiltration of these cells globally throughout the brain parenchyma (Fig. 3 E-H). Neuroinflammation is associated with characteristic T cell signature in the brain (*36*); our transcriptomic data showed the upregulation of the chemokine CXCL16, which is consistent with this recruitment of T cells and with the cytokine pattern of chronic inflammation with the increased

expression of *INFG* and *TNF* (*37*). The protein products of these genes, IFN-γ and TNFα, would induce the secretion of CXCL16 (*38*, *39*). Transcriptionally, we also observed increased expression of *IL6* and *TGFB1*, both necessary for the differentiation of Th17 cells from Th1 cells. The cytokine *IL23* was also upregulated, which, via IL-23R, can induce secretion of IL17 from Th 17 cells (*40*, *41*).

Infiltrating monocytes also showed an inflammatory signature in the Aldara model of neuroinflammation (reviewed by *42–45*). Furthermore, there is an intriguing relationship between Th17/IL17 and inflammation-induced behaviours. IL-17A receptors are expressed by excitatory glutaminergic neurons of the medial prefrontal cortex (*46*). Genetic ablation of these receptors in mice results in the differential expression of genes known to be dysregulated in human depression (reviewed by *47*). Moreover, elevated IL-17A expression has been shown to generate depressive-like behaviour in murine models and Th17 cells accumulate in the brains of mice exhibiting learned helplessness (*47*). Clinically, depressed patients have increased levels of peripheral blood Th17 cells, highest in those at increased suicide risk (*48*).

We also noted B cell upregulation in response to Aldara treatment. Stress has been shown to be associated with activation of IL10-producing B cells and terminally differentiated B cells (plasma cells); B cells may influence behaviour by regulating meningeal myeloid cell activation controlling the magnitude of IFNγ signalling in the meninges (*49*). Systematic reviews have noted increased NK cells and B cells in the circulation of depressed patients (*50*). Furthermore, an association has been reported between higher leukocyte count and depression severity; in particular, higher NK cells, higher CD4/CD8 ratio and Th17/Treg ratio (*51*).

Regarding myeloid cells, recent studies have linked recruitment of peripheral monocytes into the brain to deficits in behaviour associated with sickness behaviour (reviewed by *42*). Among these studies, Garré et al, demonstrated cognitive impairments and neurite remodelling attributable solely to circulating CX3CR1+ monocyte-derived TNFα (*43*). Similarly, $CCR2^{+}$ monocytes infiltrating CNS are a primary source of IL6 following cerebrovascular injury (*44*). Clinically, IFNγ

production in the context of stress-induced anxiety leads to activation of myeloid cells; IFNγ also activates the choroid plexus to promote leukocyte recruitment to the brain following injury (*45*).

We used a combination of whole-brain transcriptomics, immunohistochemistry and flow cytometry to interrogate the response of microglia and astrocytes in terms of gene expression, morphological and immunological changes. These multiple lines of evidence converged on the conclusion that both cell types play a key role in mediating neuroinflammatory responses to Aldara. At the transcriptional level, we upregulation of the microglia genes: *TMEM119*, *HEXB*, *MSR1*, *CD68*, and *MERTK*, which have been implicated in microglial activation (*52*). And with flow cytometry we show microglia to be activated with increased expression of macrophage like makers e.g. MHCII, F4/80 and MSR1 and an overall increase in number of microglia. Recent work by others has shown that microglia can rapidly proliferate and turn over (*53*), so our data would suggest that this can happen very quickly in response to neuroinflammation. These activated microglia are also a source of proinflammatory cytokines such as TNFα, IL6 and IFNγ (reviewed by *54*)

We also saw upregulation of several astrocyte marker genes, *GFAP*, *AQP4*, *ALDH1L1*, *MGST1*, *FAM107A*, and *SLC1A3*, changes in the expression of which are involved in astrocytic activation (*55*). Immunohistochemistry revealed no morphological changes associated with astrocytes, at least using GFAP as a marker (Fig 4). While flow cytometry revealed no change in astrocyte number (Fig 4), we used a triple positive marker approach to quantify activated astrocytes with GFAP, S100β and ASCA2 as flow cytometry makers. Despite a lack of apparent astrocytic morphological change, we found that astrocytes significantly increased production of the proinflammatory cytokines IL-6 and IFN-γ. *In vitro* culture experiments using human astrocytoma cells show an association between IL17 and astrocyte activation (*56*). Astrocytes express both IL-17A and IL-17C receptors, and *in vitro* treatment of these cells with IL-17A increases protein levels of other proinflammatory cytokines, particularly IL-6 and TNFα (*57*). Given that astrocytes were producing these proinflammatory cytokines, we conclude that they were in an activate state despite lacking any obvious morphological

change. This reinforces the conclusion that one cannot draw strong conclusions about astrocyte function using morphology alone, or by using GFAP alone to study this enigmatic cell type.

Recent work has identified a role for activated microglia in inducing astrocytes via secretion of Il-1α, TNFα, and C1q (*58*). More recent work has further detailed subsets of reactive astrocytes defined by interferon-responsive genes such as *Igtp*, *Mx1* and *Ifit3* – classifying these as interferon-responsive astrocytes (*55*). We found these genes to be significantly upregulated in treated vs control brains (see supplementary material). Interferon signalling in astrocytes is important for anti-viral immune responses, regulating synaptic plasticity and glutamate transport mechanism (a pathway downregulated in our transcriptomic dataset). Given that we found an interferon response to Aldara, a plausible mechanism is that the interferon pathway, acting through astrocytes, links immune activation with downstream effects on glutamatergic neurotransmission.

Altered excitatory neurotransmission

Glutamate plays a potentially salient mechanistic role in the interface between cytokines and neural activity, as proinflammatory cytokines modulate both glutamate release and reuptake mechanisms at the synaptic level. Astrocytes, forming an interconnected syncytium throughout the brain, play a key role in cycling neurotransmitters such as glutamate through mechanisms, such as transmitter reuptake (*59*, *60*). Proinflammatory cytokines such as IFNγ, IL-17A, TNF and IL6 amplify and alter the magnitude and propagation of intracellular Ca^{2+} oscillations in astrocytes, and increased levels of these cytokines are associated with perturbed glutamatergic neurotransmission After 3 days of Aldara treatment, we found that the magnitude of the evoked thalamic AMPA receptor-mediated EPSC onto ventral MSNs was substantially reduced compared to control-treated mice, but without any change to the AMPA/NMDA ratio nor change in the frequency of amplitude of spontaneous EPSPs. The lack of change in AMPA/NMDA ratio would suggest the change in amplitude of the thalamic input is not a result of synaptic plasticity such as LTD (*61*, *62*). We did not use TTX to determine whether the spontaneous events we observed were sEPSCs (driven by action potential activity in the slices) or mEPSCs (TTX-resistant events driven by spontaneous vesicle release from

presynaptic terminals). However, our *ex vivo* slice orientation would suggest that few corticostriatal or thalamostriatal projections would be intact and others have found that sEPSCs in striatum tend to be TTX-resistant (*63*) so we interpret our sEPSC data to indicate that no overall change in presynaptic neurotransmitter release occurs in the slices.

We hypothesise that the changes in evoked thalamic EPSC onto ventral MSNs may be the result of receptor internalisation due to prolonged exposure to increased glutamate due to the influence of inflammatory molecules on astrocytes. Transcriptomic data revealed reductions in Homer1, which is involved in AMPA receptor homeostatic scaling (*29*), as well as downregulation of glutamate-gated ion channels. A possible mechanism driving increased extrasynaptic glutamate is via an increase in surface expression of cysteine/glutamate exchanger transporters that extrude glutamate into the extra synaptic space in exchange for cysteine (reviewed by *64*). These transporters release large volumes of glutamate near extra synaptic NMDA receptors. Conversely, inflammation decreases astrocytic clearance and buffering of glutamate by downregulation of glutamate transporters (*64*). Our observed downregulation of the astrocytic glutamate transporter *EAAT2* is consistent with this. We found no change in the transcription of genes associated with GABAergic signalling.

We observed robust c-Fos expression in midline thalamus just 4 hours after IMQ treatment (Fig. 6) and the ventral striatum, including nucleus accumbens (NAcc), is key to reward circuitry and to motivation, as it translates motivation to action in goal directed behaviours receiving glutamatergic input from both thalamus and cortical regions that help regulate such behaviours (*65*). So, it is certainly tempting to speculate that impaired thalamostriatal signalling is one the of the mechanisms underlying inflammation-induced anhedonic and depressive behaviours. In humans, the phenomenon of reward prediction error (RPE) is critical for regulating adaptive motivated behaviours by updating the expected value (that is, the appetitive worth) of different choice/decision alternatives that lead to either positive or negative outcomes. Neuronal firing in the NAcc has been linked to RPE signals that reflect the difference between expected and actual rewards. At the cognitive level, mis-estimation of expected value due to diminished RPE signalling has offered a potential explanation of

depressive symptoms, such as anhedonia (*66*). Moreover, anhedonia is associated with blunted RPE striatal activity during reward learning (*67*). Further clinical neuroimaging studies correlated inflammation (and anhedonia) with blunted striatal RPEs (*68*) and reduced fronto-striatal functional connectivity in humans (*69*).

Limitations to the model

We have previously demonstrated that IMQ enters the brain and directly drives neuroinflammation via activation of TLR7. However, IMQ (especially when formulated with isostearic acid in Aldara cream) can also cause a peripheral inflammatory response by driving a psoriasis-like skin inflammation (*70*). As such, the neuroinflammatory response has two potential drivers: the direct effects of IMQ on the brain and the effects of peripheral inflammation via neural and humoral routes, and these two may act synergistically (*70*). It is not possible in this study to separate these two different inflammatory pathways although we do not believe that this is a significant confounding factor for interpreting our results, given that most humans experiencing psychiatric symptoms due to inflammatory disease will likely experience both central and peripheral inflammation.

Conclusions

Overall, this model of neuroinflammation results in upregulation of key cytokine and chemokine pathways leading to microglia and astrocyte activation and the recruitment of activated immune cells to the brain. The T cell recruitment results in Th1/Th17 differentiation and a pattern of widespread chemokine and cytokine upregulation. Neurobiologically, this inflammatory response results in reduced excitability of ventral striatum to midline thalamic input and the expression of behaviours that are suggestive of reduced motivation or anhedonia but without an increase in anxiety. The reward behaviour abnormalities could be construed as being driven by perturbed glutamatergic neurotransmission in the ventral striatum, possibly driven by receptor internalisation or downregulation as a homeostatic response to increased extracellular glutamate concentration caused by impaired astrocytic reuptake mechanisms. Our study provides strong evidence for the utility of the Aldara model as non-invasive model of neuroinflammation leading to reward-related

behavioural abnormalities. This will aid understanding of the mechanisms underlying inflammation-induced neuropsychiatric phenotypes including depression.

Acknowledgements

We gratefully acknowledge the support of the Inger M Lilya and George Simpson Biological Psychiatry Scholarships. This work was supported by PhD studentships from the Saudi Arabia Ministry of Science (HAF) and the Government of Turkey (YK). The authors gratefully acknowledge the Glasgow Imaging Facility for their support and assurance in this work. The authors gratefully acknowledge the Flow Core Facility of the University of Glasgow for their support & assistance in this work. For the purpose of open access, the authors have applied a Creative Commons Attribution (CC-BY) licence to any Author Accepted Manuscript version arising from this submission.

Reference

1. H. S. Kwon, S.-H. Koh, Neuroinflammation in neurodegenerative disorders: the roles of microglia and astrocytes. *Transl. Neurodegener.* **9**, 42 (2020).

2. N. Müller, E. Weidinger, B. Leitner, M. J. Schwarz, The role of inflammation in schizophrenia. *Front. Neurosci.* **9**, 372 (2015).

3. R. L. Jayaraj, S. Azimullah, R. Beiram, F. Y. Jalal, G. A. Rosenberg, Neuroinflammation: friend and foe for ischemic stroke. *J. Neuroinflammation* **16**, 142 (2019).

4. L. Nerurkar, S. Siebert, I. B. McInnes, J. Cavanagh, Rheumatoid arthritis and depression: an inflammatory perspective. *Lancet Psychiatry* **6**, 164–173 (2019).

5. J. Brock, N. Basu, J. C. M. Schlachetzki, G. Schett, I. B. McInnes, J. Cavanagh, Immune mechanisms of depression in rheumatoid arthritis. *Nat. Rev. Rheumatol.* **19**, 790–804 (2023).

6. A. J. Grippo, J. Francis, T. G. Beltz, R. B. Felder, A. K. Johnson, Neuroendocrine and cytokine profile of chronic mild stress-induced anhedonia. *Physiol. Behav.* **84**, 697–706 (2005).

7. R. Yin, K. Zhang, Y. Li, Z. Tang, R. Zheng, Y. Ma, Z. Chen, N. Lei, L. Xiong, P. Guo, G. Li, Y. Xie, Lipopolysaccharide-induced depression-like model in mice: meta-analysis and systematic evaluation. *Front. Immunol.* **14**, 1181973 (2023).

8. S. M. Fine, R. A. Angel, S. W. Perry, L. G. Epstein, J. D. Rothstein, S. Dewhurst, H. A. Gelbard, Tumor Necrosis Factor α Inhibits Glutamate Uptake by Primary Human Astrocytes IMPLICATIONS FOR PATHOGENESIS OF HIV-1 DEMENTIA*. *J. Biol. Chem.* **271**, 15303–15306 (1996).

9. H. Takeuchi, S. Jin, J. Wang, G. Zhang, J. Kawanokuchi, R. Kuno, Y. Sonobe, T. Mizuno, A. Suzumura, Tumor Necrosis Factor-α Induces Neurotoxicity via Glutamate Release from

Hemichannels of Activated Microglia in an Autocrine Manner*. *J. Biol. Chem.* **281**, 21362–21368 (2006).

10. D. Stellwagen, E. C. Beattie, J. Y. Seo, R. C. Malenka, Differential Regulation of AMPA Receptor and GABA Receptor Trafficking by Tumor Necrosis Factor-α. *J. Neurosci.* **25**, 3219–3228 (2005).

11. A. McColl, C. A. Thomson, L. Nerurkar, G. J. Graham, J. Cavanagh, TLR7-mediated skin inflammation remotely triggers chemokine expression and leukocyte accumulation in the brain. *J. Neuroinflammation* **13**, 102 (2016).

12. F. Faul, E. Erdfelder, A.-G. Lang, A. Buchner, G*Power 3: A flexible statistical power analysis program for the social, behavioral, and biomedical sciences. *Behav Res Methods* **39**, 175–191 (2007).

13. D. Kim, J. M. Paggi, C. Park, C. Bennett, S. L. Salzberg, Graph-based genome alignment and genotyping with HISAT2 and HISAT-genotype. *Nat. Biotechnol.* **37**, 907–915 (2019).

14. M. I. Love, W. Huber, S. Anders, Moderated estimation of fold change and dispersion for RNA-seq data with DESeq2. *Genome Biol.* **15**, 550 (2014).

15. J. J. Cole, B. A. Faydaci, D. McGuinness, R. Shaw, R. A. Maciewicz, N. A. Robertson, C. S. Goodyear, Searchlight: automated bulk RNA-seq exploration and visualisation using dynamically generated R scripts. *BMC Bioinform.* **22**, 411 (2021).

16. L. Kolberg, U. Raudvere, I. Kuzmin, P. Adler, J. Vilo, H. Peterson, g:Profiler—interoperable web service for functional enrichment analysis and gene identifier mapping (2023 update). *Nucleic Acids Res.* **51**, W207–W212 (2023).

17. L. Kolberg, U. Raudvere, I. Kuzmin, J. Vilo, H. Peterson, gprofiler2 -- an R package for gene list functional enrichment analysis and namespace conversion toolset g:Profiler. *F1000Research* **9**, ELIXIR-709 (2020).

18. J. Schindelin, I. Arganda-Carreras, E. Frise, V. Kaynig, M. Longair, T. Pietzsch, S. Preibisch, C. Rueden, S. Saalfeld, B. Schmid, J.-Y. Tinevez, D. J. White, V. Hartenstein, K. Eliceiri, P. Tomancak, A. Cardona, Fiji: an open-source platform for biological-image analysis. *Nat Methods* **9**, 676–682 (2012).

19. H. W. Berendse, H. J. Groenewegen, Organization of the thalamostriatal projections in the rat, with special emphasis on the ventral striatum. *J. Comp. Neurol.* **299**, 187–228 (1990).

20. R. M. Deacon, Assessing nest building in mice. *Nat. Protoc.* **1**, 1117–1119 (2006).

21. M. Kanehisa, M. Furumichi, Y. Sato, M. Kawashima, M. Ishiguro-Watanabe, KEGG for taxonomy-based analysis of pathways and genomes. *Nucleic Acids Res.* **51**, D587–D592 (2022).

22. B. Jassal, L. Matthews, G. Viteri, C. Gong, P. Lorente, A. Fabregat, K. Sidiropoulos, J. Cook, M. Gillespie, R. Haw, F. Loney, B. May, M. Milacic, K. Rothfels, C. Sevilla, V. Shamovsky, S. Shorser, T. Varusai, J. Weiser, G. Wu, L. Stein, H. Hermjakob, P. D'Eustachio, The reactome pathway knowledgebase. *Nucleic Acids Res.* **48**, D498–D503 (2019).

23. A. R. Pico, T. Kelder, M. P. van Iersel, K. Hanspers, B. R. Conklin, C. Evelo, WikiPathways: Pathway Editing for the People. *PLoS Biol.* **6**, e184 (2008).

24. M. A. Harris, J. Clark, A. Ireland, J. Lomax, M. Ashburner, R. Foulger, K. Eilbeck, S. Lewis, B. Marshall, C. Mungall, J. Richter, G. M. Rubin, J. A. Blake, C. Bult, M. Dolan, H. Drabkin, J. T. Eppig, D. P. Hill, L. Ni, M. Ringwald, R. Balakrishnan, J. M. Cherry, K. R. Christie, M. C. Costanzo, S. S. Dwight, S. Engel, D. G. Fisk, J. E. Hirschman, E. L. Hong, R. S. Nash, A. Sethuraman, C. L. Theesfeld, D. Botstein, K. Dolinski, B. Feierbach, T. Berardini, S. Mundodi, S. Y. Rhee, R. Apweiler, D. Barrell, E. Camon, E. Dimmer, V. Lee, R. Chisholm, P. Gaudet, W. Kibbe, R. Kishore, E. M. Schwarz, P. Sternberg, M. Gwinn, L. Hannick, J. Wortman, M. Berriman, V. Wood, N. de la Cruz, P. Tonellato, P. Jaiswal, T. Seigfried, R. White, G. O. Consortium, The Gene Ontology (GO) database and informatics resource. *Nucleic Acids Res.* **32**, D258–D261 (2004).

25. B. Korin, T. L. Ben-Shaanan, M. Schiller, T. Dubovik, H. Azulay-Debby, N. T. Boshnak, T. Koren, A. Rolls, High-dimensional, single-cell characterization of the brain's immune compartment. *Nat. Neurosci.* **20**, 1300–1309 (2017).

26. I. C. M. Hoogland, C. Houbolt, D. J. van Westerloo, W. A. van Gool, D. van de Beek, Systemic inflammation and microglial activation: systematic review of animal experiments. *J. Neuroinflammation* **12**, 114 (2015).

27. L. Nerurkar, A. McColl, G. Graham, J. Cavanagh, The Systemic Response to Topical Aldara Treatment is Mediated Through Direct TLR7 Stimulation as Imiquimod Enters the Circulation. *Sci. Rep.* **7**, 16570 (2017).

28. N. C. Klapoetke, Y. Murata, S. S. Kim, S. R. Pulver, A. Birdsey-Benson, Y. K. Cho, T. K. Morimoto, A. S. Chuong, E. J. Carpenter, Z. Tian, J. Wang, Y. Xie, Z. Yan, Y. Zhang, B. Y. Chow, B. Surek, M. Melkonian, V. Jayaraman, M. Constantine-Paton, G. K.-S. Wong, E. S. Boyden, Independent optical excitation of distinct neural populations. *Nat Methods* **11**, 338–346 (2014).

29. N. E. Clifton, S. Trent, K. L. Thomas, J. Hall, Regulation and Function of Activity-Dependent Homer in Synaptic Plasticity. *Mol. Neuropsychiatry* **5**, 147–161 (2019).

30. S. Scheggi, M. G. D. Montis, C. Gambarana, Making Sense of Rodent Models of Anhedonia. *Int. J. Neuropsychopharmacol.* **21**, 1049–1065 (2018).

31. L. Ma, K. A. Demin, T. O. Kolesnikova, S. L. Kharsko, X. Zhu, X. Yuan, C. Song, D. A. Meshalkina, B. E. Leonard, L. Tian, A. V. Kalueff, Animal inflammation-based models of depression and their application to drug discovery. *Expert Opin. Drug Discov.* **12**, 995–1009 (2017).

32. N. H. Kalin, The Critical Relationship Between Anxiety and Depression. *Am. J. Psychiatry* **177**, 365–367 (2020).

33. C. A. Thomson, A. McColl, J. Cavanagh, G. J. Graham, Peripheral inflammation is associated with remote global gene expression changes in the brain. *J. Neuroinflammation* **11**, 73 (2014).

34. H. Konishi, H. Kiyama, Microglial TREM2/DAP12 Signaling: A Double-Edged Sword in Neural Diseases. *Front. Cell. Neurosci.* **12**, 206 (2018).

35. M. Audrain, J. Haure-Mirande, J. Mleczko, M. Wang, J. K. Griffin, P. H. S. George-Hyslop, P. Fraser, B. Zhang, S. Gandy, M. E. Ehrlich, Reactive or transgenic increase in microglial TYROBP reveals a TREM2-independent TYROBP–APOE link in wild-type and Alzheimer's-related mice. *Alzheimer's Dement.* **17**, 149–163 (2021).

36. V. Cipollini, J. Anrather, F. Orzi, C. Iadecola, Th17 and Cognitive Impairment: Possible Mechanisms of Action. *Front. Neuroanat.* **13**, 95 (2019).

37. S. F. Rosen, A. L. Soung, W. Yang, S. Ai, M. Kanmogne, V. A. Davé, M. Artyomov, J. A. Magee, R. S. Klein, Single-cell RNA transcriptome analysis of CNS immune cells reveals CXCL16/CXCR6 as maintenance factors for tissue-resident T cells that drive synapse elimination. *Genome Med.* **14**, 108 (2022).

38. L. Veinotte, S. Gebremeskel, B. Johnston, CXCL16-positive dendritic cells enhance invariant natural killer T cell-dependent IFNγ production and tumor control. *OncoImmunology* **5**, e1160979 (2016).

39. J.-Y. Kee, A. Ito, S. Hojo, I. Hashimoto, Y. Igarashi, K. Tsuneyama, K. Tsukada, T. Irimura, N. Shibahara, I. Takasaki, A. Inujima, T. Nakayama, O. Yoshie, H. Sakurai, I. Saiki, K. Koizumi, CXCL16 suppresses liver metastasis of colorectal cancer by promoting TNF-α-induced apoptosis by tumor-associated macrophages. *BMC Cancer* **14**, 949 (2014).

40. S. Aggarwal, N. Ghilardi, M.-H. Xie, F. J. de Sauvage, A. L. Gurney, Interleukin-23 Promotes a Distinct CD4 T Cell Activation State Characterized by the Production of Interleukin-17*. *J. Biol. Chem.* **278**, 1910–1914 (2003).

41. P. R. Mangan, L. E. Harrington, D. B. O'Quinn, W. S. Helms, D. C. Bullard, C. O. Elson, R. D. Hatton, S. M. Wahl, T. R. Schoeb, C. T. Weaver, Transforming growth factor-β induces development of the TH17 lineage. *Nature* **441**, 231–234 (2006).

42. E. S. Wohleb, D. B. McKim, J. F. Sheridan, J. P. Godbout, Monocyte trafficking to the brain with stress and inflammation: a novel axis of immune-to-brain communication that influences mood and behavior. *Front. Neurosci.* **8**, 447 (2015).

43. J. M. Garré, H. M. Silva, J. J. Lafaille, G. Yang, CX3CR1+ monocytes modulate learning and learning-dependent dendritic spine remodeling via TNF-α. *Nat Med* **23**, 714–722 (2017).

44. B.-R. Choi, K. R. Johnson, D. Maric, D. B. McGavern, Monocyte-derived IL-6 programs microglia to rebuild damaged brain vasculature. *Nat. Immunol.* **24**, 1110–1123 (2023).

45. G. Kunis, K. Baruch, N. Rosenzweig, A. Kertser, O. Miller, T. Berkutzki, M. Schwartz, IFN-γ-dependent activation of the brain's choroid plexus for CNS immune surveillance and repair. *Brain* **136**, 3427–3440 (2013).

46. K. A. de Lima, J. Rustenhoven, S. D. Mesquita, M. Wall, A. F. Salvador, I. Smirnov, G. M. Cebinelli, T. Mamuladze, W. Baker, Z. Papadopoulos, M. B. Lopes, W. S. Cao, X. S. Xie, J. Herz, J. Kipnis, Meningeal γδ T cells regulate anxiety-like behavior via IL-17a signaling in neurons. *Nat. Immunol.* **21**, 1421–1429 (2020).

47. E. Beurel, J. A. Lowell, Th17 cells in depression. *Brain, Behav., Immun.* **69**, 28–34 (2018).

48. C. Schiweck, M. Valles-Colomer, V. Arolt, N. Müller, J. Raes, A. Wijkhuijs, S. Claes, H. Drexhage, E. Vrieze, Depression and suicidality: A link to premature T helper cell aging and increased Th17 cells. *Brain, Behav., Immun.* **87**, 603–609 (2020).

49. M.-E. Lynall, S. L. Kigar, M. L. Lehmann, A. E. DePuyt, Z. K. Tuong, S. J. Listwak, A. G. Elkahloun, E. T. Bullmore, M. Herkenham, M. R. Clatworthy, B-cells are abnormal in psychosocial stress and regulate meningeal myeloid cell activation. *Brain, Behav., Immun.* **97**, 226–238 (2021).

50. É. M. Foley, J. T. Parkinson, R. E. Mitchell, L. Turner, G. M. Khandaker, Peripheral blood cellular immunophenotype in depression: a systematic review and meta-analysis. *Mol. Psychiatry* **28**, 1004–1019 (2023).

51. N. V. Sørensen, B. H. Frandsen, S. Orlovska-Waast, T. B. Buus, N. Ødum, R. H. Christensen, M. E. Benros, Immune cell composition in unipolar depression: a comprehensive systematic review and meta-analysis. *Mol. Psychiatry* **28**, 391–401 (2023).

52. K. Borst, A. A. Dumas, M. Prinz, Microglia: Immune and non-immune functions. *Immunity* **54**, 2194–2208 (2021).

53. K. Askew, K. Li, A. Olmos-Alonso, F. Garcia-Moreno, Y. Liang, P. Richardson, T. Tipton, M. A. Chapman, K. Riecken, S. Beccari, A. Sierra, Z. Molnár, M. S. Cragg, O. Garaschuk, V. H. Perry, D. Gomez-Nicola, Coupled Proliferation and Apoptosis Maintain the Rapid Turnover of Microglia in the Adult Brain. *Cell Rep.* **18**, 391–405 (2017).

54. U. Hanisch, Microglia as a source and target of cytokines. *Glia* **40**, 140–155 (2002).

55. P. Prakash, H. Erdjument-Bromage, M. R. O'Dea, C. N. Munson, D. Labib, V. Fossati, T. A. Neubert, S. A. Liddelow, Proteomic profiling of interferon-responsive reactive astrocytes in rodent and human. *Glia* **72**, 625–642 (2024).

56. T. You, Y. Bi, J. li, M. Zhang, X. Chen, K. Zhang, J. Li, IL-17 induces reactive astrocytes and up-regulation of vascular endothelial growth factor (VEGF) through JAK/STAT signaling. *Sci. Rep.* **7**, 41779 (2017).

57. M. Kostic, N. Zivkovic, A. Cvetanovic, I. Stojanovic, M. Colic, IL-17 signalling in astrocytes promotes glutamate excitotoxicity: Indications for the link between inflammatory and neurodegenerative events in multiple sclerosis. *Mult. Scler. Relat. Disord.* **11**, 12–17 (2017).

58. S. A. Liddelow, K. A. Guttenplan, L. E. Clarke, F. C. Bennett, C. J. Bohlen, L. Schirmer, M. L. Bennett, A. E. Münch, W.-S. Chung, T. C. Peterson, D. K. Wilton, A. Frouin, B. A. Napier, N. Panicker, M. Kumar, M. S. Buckwalter, D. H. Rowitch, V. L. Dawson, T. M. Dawson, B. Stevens, B. A. Barres, Neurotoxic reactive astrocytes are induced by activated microglia. *Nature* **541**, 481–487 (2017).

59. A. Araque, M. Navarrete, Glial cells in neuronal network function. *Philos. Trans. R. Soc. B: Biol. Sci.* **365**, 2375–2381 (2010).

60. G. Perea, M. Navarrete, A. Araque, Tripartite synapses: astrocytes process and control synaptic information. *Trends Neurosci* **32**, 421–431 (2009).

61. A. Citri, R. C. Malenka, Synaptic Plasticity: Multiple Forms, Functions, and Mechanisms. *Neuropsychopharmacology* **33**, 18–41 (2008).

62. M. A. Ungless, J. L. Whistler, R. C. Malenka, A. Bonci, Single cocaine exposure in vivo induces long-term potentiation in dopamine neurons. *Nature* **411**, 583–587 (2001).

63. K. Tang, M. J. Low, D. K. Grandy, D. M. Lovinger, Dopamine-dependent synaptic plasticity in striatum during in vivo development. *Proc. Natl. Acad. Sci. United States Am.* **98**, 1255–60 (2001).

64. A. Volterra, J. Meldolesi, Astrocytes, from brain glue to communication elements: the revolution continues. *Nat. Rev. Neurosci.* **6**, 626–640 (2005).

65. K. Burrows, J. L. Stewart, R. Kuplicki, L. Figueroa-Hall, P. A. Spechler, H. Zheng, S. M. Guinjoan, T. 1000 Investigators, J. B. Savitz, T. K. Teague, M. P. Paulus, Elevated peripheral inflammation is associated with attenuated striatal reward anticipation in major depressive disorder. *Brain, Behav., Immun.* **93**, 214–225 (2021).

66. Q. J. M. Huys, N. D. Daw, P. Dayan, Depression: A Decision-Theoretic Analysis. *Annu. Rev. Neurosci.* **38**, 1–23 (2015).

67. J. D. Steele, D. Christmas, M. S. Eljamel, K. Matthews, Anterior Cingulotomy for Major Depression: Clinical Outcome and Relationship to Lesion Characteristics. *Biol Psychiat* **63**, 670–677 (2008).

68. N. A. Harrison, V. Voon, M. Cercignani, E. A. Cooper, M. Pessiglione, H. D. Critchley, A Neurocomputational Account of How Inflammation Enhances Sensitivity to Punishments Versus Rewards. *Biol. Psychiatry* **80**, 73–81 (2016).

69. J. C. Felger, Z. Li, E. Haroon, B. J. Woolwine, M. Y. Jung, X. Hu, A. H. Miller, Inflammation is associated with decreased functional connectivity within corticostriatal reward circuitry in depression. *Mol. Psychiatry* **21**, 1358–1365 (2016).

70. S. Straß, J. Geiger, M. Martorelli, S. Geiger, N. Cloos, M. Keppler, T. Fischer, L. Riexinger, A. Schwamborn, J. Guezguez, N. Späth, S. Cruces, J.-H. Guse, T. L. Sandri, M. Burnet, S. Laufer, Isostearic acid is an active component of imiquimod formulations used to induce psoriaform disease models. *Inflammopharmacology* **31**, 799–812 (2023).